Models of porous, elastic and rigid materials
in moving fluids

by

Uğis Lācis

Cover: deformed solid skeleton of a porous and elastic material. The deformation is caused by a flow vortex from above the material.

"The success or failure of your deeds does not add up to the sum of your life. Your spirit cannot be weighed. Judge yourself by the intentions of your actions, and by the strength with which you faced the challenges that have stood in your way.

The Universe is vast and we are so small. There is really only one thing we can ever truly control... whether we are good or evil."

/ Oma Desala, Mother Nature, Stargate SG-1/

"I have lived many lifetimes. First... in Atlantis. Then... on Earth, before the dawn of your civilization. Then I joined the ranks of the Ascended. And finally, I returned to mortal form, to live out my remaining days among the noblemen of Arthur's Court. Or, so I thought. And through all these eons, only one thing has stayed the same: there is never enough time."

/ Merlin, Archmage of the Round, Stargate SG-1 /

Models of porous, elastic and rigid materials in moving fluids

Uğis Lācis

Linné FLOW Centre, KTH Mechanics, Royal Institute of Technology
SE-100 44 Stockholm, Sweden

Abstract

Tails, fins, scales, and surface coatings are used by organisms for various tasks, including locomotion. Since millions of years of evolution have passed, we expect that the design of surface structures is optimal for the tasks of the organism. These structures serve as an inspiration in this thesis to identify new mechanisms for flow control. There are two general categories of fluid-structure-interaction mechanisms. The first is active interaction, where an organism actively moves parts of the body or its entire body in order to modify the surrounding flow field (e.g., birds flapping their wings). The second is passive interaction, where appendages or surface textures are not actively controlled by the organism and hence no energy is spent (e.g., feathers passively moving in the surrounding flow). Our aim is to find new passive mechanisms that interact with surrounding fluids in favourable ways; for example, to increase lift and to decrease drag.

In the first part of this work, we investigate a simple model of an appendage (splitter plate) behind a bluff body (circular cylinder or sphere). If the plate is sufficiently short and there is a recirculation region behind the body, the straight position of the appendage becomes unstable, similar to how a straight vertical position of an inverted pendulum is unstable under gravity. We explain and characterize this instability using computations, experiments and a reduced-order model. The consequences of this instability are reorientation (turn) of the body and passive dispersion (drift with respect to the direction of the gravity). The observed mechanism could serve as a means to enhance locomotion and dispersion for various motile animals and non-motile seeds.

In the second part of this thesis, we look into effective models of porous and poroelastic materials. We use the method of homogenization via multi-scale expansion to model a poroelastic medium with a continuum field. In particular, we derive boundary conditions for the velocity and the pressure at the interface between the free fluid and the porous or poroelastic material. The results obtained using the derived boundary conditions are then validated with respect to direct numerical simulations (DNS) in both two-dimensional and three-dimensional settings. The continuum model – coupled with the necessary boundary conditions – gives accurate predictions for both the flow field and the displacement field when compared to DNS.

Descriptors: fluid-structure-interaction, flow control, passive appendages, homogenization, poroelastic coatings, separated flows, surface-fluid interface.

Modeller av porösa, elastiska och stela material i strömmande fluider

Uģis Lācis

Linné FLOW Centre, KTH Mekanik, Kungliga Tekniska Högskolan

SE-100 44 Stockholm, Sverige

Sammanfattning

Många djur använder sig av fjäll, päls, hår eller fjädrar för att öka sin förmåga att förflytta sig i luft eller vatten. Eftersom djuren har genomgått miljontals år av evolution, kan man förvänta sig att ytstrukturernas form är optimala för organismens uppgifter. Dessa strukturer tjänar som inspiration i denna avhandling för att identifiera nya mekanismer för manipulering av strömning.

Samverkan mellan fluider och strukturer (så kallad *fluid-struktur-interaktion*) kan delas upp i två kategorier. Den första typen av samverkan är aktiv, vilket innebär att en organism aktivt rör hela eller delar av sin kropp för att manipulera det omgivande strömningsfältet (till exempel fåglar som flaxar sina vingar). Den andra typen är passiv samverkan, där organismer har utväxter (svansar, fjärdar, etc.) eller ytbeläggningar som de inte aktivt har kontroll över och som således inte förbrukar någon energi. Ett exempel är fjädrar som passivt rör sig i det omgivande flödet. Vårt mål är att hitta nya passiva mekanismer som växelverkar med den omgivande fluiden på ett fördelaktigt sätt, exempelvis genom att öka lyftkraften eller minska luftmotståndet.

I den första delen av detta arbete undersöker vi en enkel modell för en utväxt (i form av en platta) bakom en cirkulär cylinder eller sfär. Om plattan är tillräckligt kort och om det finns ett vak bakom kroppen kommer det upprätta läget av plattan att vara instabilt. Denna instabilitet är i princip samma som uppstår då man försöker balansera en penna på fingret. Vi förklarar den bakomliggande mekanismen av denna instabilitet genom numeriska beräkningar, experiment och en enkel modell med tre frihetsgrader. Konsekvenserna av denna instabilitet är en omorientering (rotation) av kroppen och en sidledsförflyttning av kroppen i förhållande till tyngdkraftens riktning. Denna mekanism kan användas djur och frön för att öka deras förmåga att förflytta eller sprida sig i vatten eller luft.

I den andra delen av avhandlingen studerar vi modeller av porösa och elastiska material. Vi använder en mångskalig metod för att modellera det poroelastiska materialet som ett kontinuum. Vi härleder randvillkor för både hastighetsfältet och trycket på gränssnittet mellan den fria fluiden och det poroelastiska materialet. Resultaten som erhållits med de härledda randvillkoren valideras sedan genom direkta numeriska simuleringar (DNS) för både två- och tredimensionella fall. Kontinuumsmodellen av materialet kopplad genom randvillkoren till den fria strömmande fluiden predikterar strömnings- och förskjutningsfält noggrant i jämförelse med DNS.

Deskriptorer: fluid-struktur-interaktion, flödeskontroll, passiva utväxter, homogenisering, ytbeläggning, separerade strömning, ytbeläggning-strömning gränssnitt.

Preface

This thesis deals with the development of models suitable to describe interaction between the moving fluid and appendages / coatings with properties inspired by nature. This work is a direct continuation of my Licentiate thesis (ISBN 978-91-7595-427-1) and contains parts of it. A short introduction on the main ideas, objectives, and tools employed, as well as a summary of the findings are presented in the first part. The second part contains five articles. The first article is published in *Nature Communications*; the second article is published in *Journal of Computational Physics*; the third article is submitted to *Physical Review Fluids*; the fourth article is under review for publication in *Journal of Fluid Mechanics* and the fifth article will be submitted to *Proceedings of the Royal Society A*. The manuscripts are fitted to the present thesis format without changing any of the content. All images acquired externally have been released to public domain by their authors under license **CC0 1.0**, if not stated otherwise.

Paper 1. U. Lācis, N. Brosse, F. Ingremeau, A. Mazzino, F. Lundell, H. Kellay, & S. Bagheri. *Passive appendages generate drift through symmetry breaking.* Nat. Commun. **5**, 2014

Paper 2. U. Lācis, K. Taira, & S. Bagheri. *A stable fluid-structure-interaction solver for low-density rigid particles using the immersed boundary projection method.* J. Comput. Phys. **305**, 2016: 300-318

Paper 3. U. Lācis, S. Olivieri, A. Mazzino & S. Bagheri. *Passive control of a falling sphere by elliptic-shaped appendages.* Submitted to Phys. Rev. Fluids, 2016

Paper 4. U. Lācis & S. Bagheri. *A framework for computing effective boundary conditions at the interface between free fluid and a porous medium.* *4th* revision submitted to J. Fluid Mech., 2016

Paper 5. U. Lācis, G. A. Zampogna & S. Bagheri. *A computational continuum model of poroelastic beds.* Manuscript in preparation for submission to P. Roy. Soc. A – Math. Phy., 2016

December 2016, Stockholm

Uğis Lācis

vii

Division of work between authors

The main advisor for the project is Dr. Shervin Bagheri (SB). Dr. Fredrik Lundell (FL) acts as co-advisor.

Paper 1

Simulations of the freely falling body has been performed by UL. The theoretical model has been created by UL and further developed with feedback from all authors. Nicolas Brosse performed the soap film experiments of fixed cylinder with feedback from FL. Francois Ingremeau and Hamid Kellay performed the soap-film experiments of the free-hanging cylinder. Andrea Mazzino (AM) supervised the numerical simulations of the three-dimensional sphere, done by Stefano Olivieri (SO). All authors analyzed data. SB and UL wrote the paper.

Paper 2

The code originally developed by SB is extended by UL to include rigid-body dynamics. The final improvement was suggested by Kunihiko Taira (KT) to recover positive-definiteness property of all solution steps. Results were obtained and paper was written by UL with feedback from KT and SB.

Paper 3

The idea of additional three-dimensional investigations was initiated by UL. The test cases and shapes of appendages to study were selected in common discussions between UL, SB, AM and SO. UL designed the appendage shapes. The numerical simulations were carried out by SO under supervision of UL and AM. The paper was written by UL and SB and later revised by UL and SB with feedback from SO and AM.

Paper 4

The theory was developed and equations were implemented and solved by UL with feedback from SB. The paper was written by UL and SB and later revised by UL through discussions with SB. The simulation code was cleaned and released in open-source repository by UL.

Paper 5

The idea of using continuous models for poroelastic materials for flow control was conceived several years ago by Alessandro Bottaro (AB) and SB. The collaboration on the topic with AB and Giuseppe Antonio Zampogna (GAZ) was initiated by SB. The need for validation was strongly advocated by UL. The multi-scale method was suggested by AB and GAZ. The theory was developed and analysed by UL with feedback from SB and GAZ. The FreeFem++ was selected by UL as main simulation tool. The governing equations were implemented and solved by UL with feedback from SB. The results from microscale elasticity problems for cubic-symmetric material were independently validated by GAZ using OpenFOAM. The paper was written by UL and SB with feedback from GAZ.

Conferences

Part of the work in this thesis has been presented at the following international conferences. The presenting author is underlined.

<u>N. Brosse</u>, U. Lācis, F. Lundell, S. Bagheri, F. Ingremeau, H. Kellay, & A. Mazzino. *Symmetry breaking of rigid/flexible plates in bluff body wakes generates rotation and drift.* 66th Annual Meeting of APS Division of Fluid Mechanics. Pittsburgh, Pennsylvania, November 2013

<u>S. Bagheri</u>, U. Lācis, N. Brosse, F. Lundell, S. Bagheri, F. Ingremeau, H. Kellay, & A. Mazzino. *Passive appendages aid locomotion through symmetry breaking.* 67th Annual Meeting of APS Division of Fluid Mechanics. San Francisco, California, November 2014

<u>U. Lācis</u>, S. Bagheri, N. Brosse, F. Lundell, S. Bagheri, F. Ingremeau, H. Kellay, & A. Mazzino. *Symmetry breaking in 3D wake of a bluff body generates rotation and drift.* 67th Annual Meeting of APS Division of Fluid Mechanics. San Francisco, California, November 2014

<u>U. Lācis</u> & S. Bagheri. *Passive appendages in two and three dimensions generate drift through symmetry breaking.* Fluid and Elasticity. Biarritz, France, June 2015

<u>S. Bagheri</u>, U. Lācis, O. Stefano, & A. Mazzino. *Passive control of a sphere by complex-shaped appendages.* 68th Annual Meeting of APS Division of Fluid Mechanics. Boston, Massachusetts, November 2015

<u>U. Lācis</u> & S. Bagheri. *Boundary conditions between poro-elastic medium and pure fluid in multi-scale modelling.* 68th Annual Meeting of APS Division of Fluid Mechanics. Boston, Massachusetts, November 2015

<u>S. Bagheri</u> & U. Lācis. *Robust velocity boundary condition for free fluid at interface with poro-elastic medium.* Mini-Symposium on Flows over Non-Smooth Walls. London, UK, May 2016

x

Contents

Part I

Overview and summary

CHAPTER 1

Introduction and motivation

Animals currently living on earth have gone though millions of years of evolution. During all these years, the variety and function of those organisms have developed tremendously. Currently there are around 1.5 million species in the animal kingdom, covered by all sorts of skins and have a wide range of abilities. We trust that the evolution has lead to animals with optimal (Parker & Smith 1990) performance for various tasks, including but not limited to hydrodynamic interaction. This serves as a motivation for us to look in the examples from the nature.
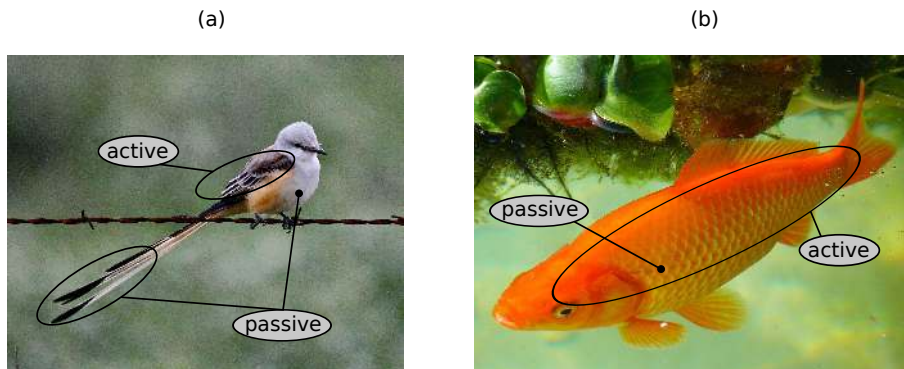

FIGURE 1.1. Examples of two motile organisms, a bird (a, Scissor-tailed Flycatcher) and a fish (b, Goldfish). The bird (a) flaps its wings actively in order to fly, while the tail and the feathers might passively improve the aerodynamical properties. The fish (b) bends its body and moves its fins actively in order to swim, while the scales might passively reduce the flow resistance.

All motile organisms interact with the surrounding environment, and most often it is fluid (birds spend most of their time time in air, while fish in water). There are two general interaction categories. The first and the most common category is active interaction. The main property of the active interaction with a fluid is that the animal must *spend energy* in order to modify the surrounding flow. The second category is passive interaction. The main property of this

category is that *energy input is not required* from the organism. Instead, an appendage or a surface structure is interacting with the flow in a coupled fluid-structure-interaction (FSI) manner. In Figure 1.1 we show a Scissor-tailed Flycatcher and a Goldfish as two examples of motile animals, which use both active and passive means to interact with the surrounding fluid. An excellent review on how swimming fishes and mammals make use of both active and passive flow control is presented by Fish & Lauder (2006).

In section 1.1, we give an overview of some identified mechanisms that living organisms use in order to interact with the surrounding fluids. Based on this overview, we outline the main aim and objectives of this thesis work in section 1.2.

FIGURE 1.2. Birds flying in a V-shaped flock.

1.1. Background

Mechanisms in *passive* and *active* categories can vary in scale and complexity. For example, a recent study by Gazzola *et al.* (2014) have provided a unified understanding of the force balance during swimming for aquatic animals with size ranging from few millimetres to tens of metres. Depending on the size, the swimmer generate around it either a laminar – ordered, simple, exhibiting low mixing – or turbulent – chaotic, complex, exhibiting high mixing – flow. Both types of flow cause pressure drag (determined by difference of pressure between front and back) and skin friction drag (determined by fluid shear or friction at the wall). The main finding of Gazzola *et al.* (2014) is that for smaller animals the surrounding flow is laminar and the generated thrust is balanced by the skin friction part of the drag, whereas for larger animals the surrounding flow is turbulent and the generated thrust is balanced by the pressure part of the drag.

Another example is the mechanism used by groups of animals, who interact with each other through modifications of surrounding fluid. A well known behaviour of various bird species is to group in flocks, as shown in Fig. 1.2. Portugal *et al.* (2014) has recently explained collective flight benefits and the underlying synchronisation mechanism of northern bald ibises. They illustrated that birds must use the complicated structures in the flow and are apparently able to synchronise wing flapping to re-use some of the energy lost in the surrounding vortex structures. These two examples falls into "active interaction" category and are large scale phenomena.

Various tails, appendages and skin coatings can be subjected to mechanisms of *passive* interaction. For example, many birds have so-called pop-up feathers, which activates during their landing. A picture of a landing swan is shown in Fig. 1.3, where active pop-up feathers are identified using red circles. The aerodynamic effect of these feathers has been investigated by Meyer *et al.* (2007). They found that the presence of these feathers can delay the dynamic stall and increase lift performance for large attack angles. This is also a large scale effect, since feathers usually pop-up in groups of many individual plumes.

FIGURE 1.3. A photo of a landing swan by Campbell (2013). Feathers that have popped up during the landing process are identified using red circles.

Another example is shark-skin that has inspired the development of riblets for aeroplanes. They are structured, fine-scale denticles on the surface. A close-up view on denticles of a lemon shark using electron microscope is shown in Fig. 1.4*a*. Dean & Bhushan (2010) have reviewed the extensive work on drag reduction function of the riblets and it is clear that a skin-friction reduction commonly up to around 5% is achievable. Bechert *et al.* (1997, 2000) have shown that for selected riblet properties, the skin-friction can be reduced even by 10%. However, riblets have not reached widespread adoption due to relatively high cost of manufacturing them and need to change the coating once

every few years. Additionally, Oeffner & Lauder (2012) have shown that the elasticity – feature which standard riblet systems usually lack – is important for increasing drag-reduction. Further on, Itoh *et al.* (2006) investigated the drag reduction properties of seal fur. A picture of seal fur on a coat is given in Fig. 1.4*b*. For closer view on the structures present in the fur, the reader is referred to the publication by Itoh *et al.* (2006). Their finding show that the seal fur is better performing than riblets. Authors argue that the reason for that is the stochastic nature of the seal fur, that is, while there is only a single wavelength present for riblets, defined by the regular geometry, the seal fur exhibits a distribution over more than one wavelength. They also point out that the role of elasticity of the seal fur is not clear and further research is needed.

(a)   (b)

FIGURE 1.4. Examples of two surface coatings. In frame (a), we show dermal denticles of a lemon shark from a scanning electron microscope, published by Deynat (2011). In frame (b), we show a close-up on a coat, which is made from seal fur.

In practice, modelling real-life materials is very challenging, because it involves working with effects at multiple scales and investigating materials that serve multiple functions. Therefore researchers have focused on different levels of abstraction in order to better isolate underlying beneficial interaction mechanisms leading to, for example, reduction of flow drag. The already mentioned riblets is one example, in which hierarchical porous and elastic structure of shark skin is modelled using simple, rigid grooves. As another example, Bagheri *et al.* (2012) have used a very simple abstraction of a real life cilia or flagella – elastic one-dimensional filament attached behind cylinder in a two-dimensional setting. They observed that in the case of long filament, the system is symmetric and the appendage flaps under the influence of the von Kármán vortex street symmetrically with respect to center line. However, if the filament is shorter than some critical length, the symmetry of the system is broken. The appendage then flaps at either top or bottom of the center line. And as a result, non-zero lift and torque is generated on the average. They attributed this

effect to resonance between the flow time scale and elasticity time scale of the filament.

Yet another example is using many filaments to coat the cylinder, as investigated by Favier *et al.* (2009). In their work, a semi-empirical homogenised model of a hairy coating is developed. They model the coating by building it from straight stiff rods, which are anchored to the cylinder by a non-linear torsion spring, and are coupled to neighbouring rods using a similar non-linear potential, based on angle difference. Then they homogenise the model and implement it numerically. By investigating various configurations, they are able to produce a drag reduction of 15% in the laminar flow regime.

Drag reduction has been successfully obtained also by production of a slip at the boundary of the fluid. The slip can be generated by, for example, hydrophobic surfaces (Tretheway & Meinhart 2002) or by introduction of microbubbles (Ushida *et al.* 2012). The slip at a wall causes smaller shear compared to no-slip at the wall, and henceforth also reduces drag. It is interesting to note that many species in nature make use of super-hydrophobic surfaces, as summarised in the review by Liu & Jiang (2011). Recently Rastegari & Akhavan (2015) investigated both laminar and turbulent flow over super-hydrophobic surfaces in a micro-channel. They show that most (at least 80%) of the drag reduction effect for turbulent flows can be attributed to the slip velocity, similar as for laminar flow. However, the remaining part (up to 20%) can be attributed to modification of turbulence itself. They also point out that if the surface would be elastic, then it is very likely that one would observe additional modifications of the turbulence and conclusions would change.

All these investigations are in general interesting and insightful, and some actually leads to beneficial interaction between surrounding flow and structures, such as drag reduction. Moreover, some of the presented examples are useful for laminar flows, and some – for turbulent flows. However, it is not presently clear, what the exact role and potential of porosity and elasticity of appendages and surfaces is for drag reduction, lift enhancement or other favourable FSI mechanisms. Currently it seems that a poroelastic coating could be useful to reduce drag for both laminar (Favier *et al.* 2009) and turbulent (Rastegari & Akhavan 2015) flows. Furthermore, majority of the available models are empirical and very simple, usually without elasticity and proper multi-scale features. For example, the thoroughly researched riblets are a crude model of shark skin without any elastic properties. Both of the objectives (see next section) in this thesis are connected to the development of models that would take multi-scale effects rigorously into account and would also be able to describe elasticity. Such models would significantly aid the understanding of the fluid-structure interaction mechanisms arising for various appendages and surfaces exposed to the fluid flow both in laminar and turbulent regime.

FIGURE 1.5. A sketch of the problems investigated in this work. In frame (a), a bluff body with an appendage is exposed to uniform free stream $\mathbf{U}_\infty$. In frame (b), a poroelastic (PE) structure is added on top of a rigid wall, which is exposed to a free fluid flow above it.

1.2. Objectives of this work

The overarching aim of this thesis is to identify new passive fluid-structure interaction mechanisms that can be used to manipulate a surrounding flowing fluid in a desirable manner. To reach this aim, we set the following two objectives:

1. Investigate theoretically and numerically the symmetry-breaking instability that arises when a single appendage – attached behind a bluff body – interacts with an incoming flow (Fig. 1.5a). Explain the physical mechanism behind this symmetry breaking and characterize the consequences of the instability for rigid particles moving in fluids.

2. Develop an effective (averaged) continuum model of a porous and elastic material attached to a rigid wall exposed to a free vortical flow from above (Fig. 1.5b). Validate the derived model with fully-resolved direct numerical simulations in two and three dimensions. Explain the transfer of mass, momentum and stress across the interface between the free fluid and the poroelastic medium.

CHAPTER 2

Research methods

In this chapter, we introduce the research methods used in order to approach the objectives outlined for this thesis. In the following sections, we describe the basics of theoretical, numerical and experimental investigations. We keep the contents of this chapter general, while occasionally emphasizing the specific methods which are employed during this thesis work.

2.1. Theoretical approaches

In order to employ theoretical investigation of a given system, one is required to develop a viable model. A reasonable model is also a prerequisite of any numerical investigation, as well as experimental observation. A theoretical model provides equations for the numerical community to solve. Without the governing equations, no investigations could be carried out. Additionally, theoretical models provide understanding of necessary measurements for experiments, as well as functions of measurement tools. Without measurement tools, experiments can not be carried out. Theoretical foundations are therefore crucial for any problem in question.

The investigation of passive flow control mechanisms found in nature is multidisciplinary. In order to describe the behaviour of the surrounding fluid, models from fluid dynamics must be invoked. To describe tails or feathers of animals, deformation must be characterised using solid mechanics models. To capture the properties of the deforming natural bodies, one has to look into biology and find, for example, how the elastic properties of a given tissue depend on the surrounding conditions. In this work, we focus on fluid mechanics and solid mechanics, and neglect more detailed biological description. Additionally, we consider theoretical approaches, which simplify the more general governing models by employing homogenisation and description of effective quantities in multi-scale systems.

2.1.1. *Fluid mechanics*

In fluid mechanics, it is common to investigate a moving fluid (flow) in a continuous manner. An example of a flow is shown in Figure 2.1. A continuum model of moving fluid is devised as follows. A velocity value $\mathbf{u}$ is assigned to a fluid parcel; the fluid parcel must be sufficiently large from microscopic point of view, such that movement of individual molecules or atoms is not important; and at the same time sufficiently small from macroscopic point of view,

FIGURE 2.1. An example of an incompressible fluid flow. Water flows in a narrow passage of a river, during which a very chaotic patterns can be seen.

such that the system of interest is composed of infinitely many fluid parcels. The conservation laws for these fluid parcels are then formulated in an integral form (summing contribution over finite volume) and finally point-wise models are created.

In this work we look at flow, which is assumed to be incompressible. This assumption holds for most of liquids, and also for gases, in which the flow speed is significantly smaller (below 30%) compared to speed of sound in that fluid. The resulting model for the fluid under those assumptions is the incompressible Navier-Stokes equations

$$\rho \left[\frac{\partial \mathbf{u}}{\partial t} + \left(\mathbf{u} \cdot \boldsymbol{\nabla} \right) \mathbf{u} \right] = -\boldsymbol{\nabla} p + \mu \nabla^2 \mathbf{u}, \tag{2.1}$$

$$\boldsymbol{\nabla} \cdot \mathbf{u} = 0, \tag{2.2}$$

$$f \left(\mathbf{u}, p \right)|_{\partial \Omega} = \mathbf{g}_{\text{BC}}, \tag{2.3}$$

where ρ is the fluid density, $\mathbf{u}$ is the velocity field, p is the pressure, μ is the dynamic viscosity of the fluid, $f\left(\mathbf{u}, p\right)|_{\partial \Omega}$ is a general function of boundary velocity and pressure values and $\mathbf{g}_{\text{BC}}$ is a general boundary condition on a surface of a fluid domain (can be both prescribed velocity or surface stress). The dimensionless Reynolds number is defined as $Re = \rho U L / \mu$, where L is a characteristic length scale of the flow. The Reynolds number characterises the ratio between inertial and viscous forces in the flow.

The Navier-Stokes equations are non-linear partial differential equations. Analytic solutions are available only for a very limited set of problems. Therefore it is common to conduct numerical (section 2.2) or experimental (section 2.3) investigations.

2.1.2. *Solid mechanics*

In solid mechanics, one of the simplest possible models of a body is a finite-sized non-deformable body with mass subjected to external forces. In such a framework, the body dynamics are very simple. For any arbitrary body there are 6 degrees of freedom in three dimensions (translation in three directions, rotation around three axis). Velocities are assigned to the center of the mass of the body and the motion is governed by the total force on the body. In a two-dimensional setting, Newton's equations of a rigid body motion surrounded by fluid are

$$\frac{\mathrm{d}\mathbf{u}_s}{\mathrm{d}t} = \frac{1}{\rho V_s} \oint_S \boldsymbol{\tau} \cdot \hat{n} \, \mathrm{d}S + \left(1 - \frac{1}{\rho}\right) g\hat{g}, \tag{2.4}$$

$$\frac{\mathrm{d}\omega_s}{\mathrm{d}t} = \frac{1}{\rho I_s} \oint_S \mathbf{r} \times (\boldsymbol{\tau} \cdot \hat{n}) \, \mathrm{d}S, \tag{2.5}$$

where $\boldsymbol{\tau}$ is the fluid stress tensor, $\mathbf{u}_s$ is the translation velocity, ω_s is the angular velocity, $\mathbf{r}$ is the radius from the center of mass to the surface of the body, $V_s = \int dV$ is a dimensionless volume, $I_s = \int \mathbf{r}^2 \, dV$ is a dimensionless moment of inertia, and $\partial\Omega_{fs} = S$ is the solid object surface. Hats are used to denote unit-vectors, here $\hat{n}$ is the unit surface-normal vector and $\hat{g}$ is a unit vector in the direction of gravity. Nevertheless, solid bodies are often deformable, which is also the case for the problems we aim to investigate. A simple example of a deforming solid body is a ruler placed on a table, and bent by forces acting at the end of the ruler and at the center of the ruler (see Figure 2.2).

The deformation is described in a continuous manner using a displacement field $\mathbf{v} = \mathbf{x} - \mathbf{x}_0$ for each solid body element (similarly as velocity field for the fluid), which is the difference between the current position $\mathbf{x}$ and initial (rest) position $\mathbf{x}_0$ in the coordinate system moving together with the center of mass of the body. In the deformed case the limited number of degrees of freedom have been replaced by a continuous field.

FIGURE 2.2. A deformed ruler caused by forces applied at both ends of the ruler as well as at the center of the ruler (reactive force form the table).

The strain of the solid body is translated to stress through a given stress-strain relationship. In this work we look at linear elasticity, i.e., in which the relation between strain and stress is a linear function. The governing equation for deformation of a solid body is then

$$\rho_s \frac{\mathrm{d}^2 \mathbf{v}}{\mathrm{d} t^2} = \nabla \cdot \left[\mathbf{C}^{\mathrm{sk}} : \frac{1}{2} \left\{ \boldsymbol{\nabla} \mathbf{v} + (\boldsymbol{\nabla} \mathbf{v})^T \right\} \right] + \mathbf{F},$$

$$\text{B.C.}\quad \mathbf{F}_b = \left[\mathbf{C}^{\mathrm{sk}} : \frac{1}{2} \left\{ \boldsymbol{\nabla} \mathbf{v} + (\boldsymbol{\nabla} \mathbf{v})^T \right\} \right] \cdot \hat{n}, \tag{2.6}$$

$$\text{I.C.}\quad \frac{1}{V} \int \mathbf{v}\, dV = \mathbf{v}_c\left(t\right), \quad \frac{1}{V} \int \mathbf{r} \times \mathbf{v}\, dV = \theta_c\left(t\right),$$

where ρ_s is the density of the structure, $\mathbf{C}^{\mathrm{sk}}$ is a fourth-rank tensor, which relates strain and stress of the structure, $\mathbf{F}$ is a body force within the structure, $\mathbf{F}_b$ is the prescribed boundary forcing, needed to determine the boundary condition at the surface. Finally, $\mathbf{v}_c$ and θ_c are the prescribed position and turn of the center of mass, which are necessary integral conditions on the displacement field values in order to render the solution unique. It is also possible to replace the integral condition with point constraints or Dirichlet boundary conditions at part of the solid body surface. If part of the boundary is specified using a known displacement value, then equations of the rigid body motion become redundant.

2.1.3. Multi-scale and homogenisation techniques

Often it is not possible to resolve all scales computationally by solving the governing equations, which are valid everywhere. Therefore, various modelling techniques, called multi-scale methods that simplify the task have been lately drawing a lot of attention (Keyes *et al.* 2013). For most of these methods, the problem in question must exhibit scale separation. That is, there has to be a small pore-scale with length l and a large system scale with length H, such that $l/H \ll 1$. A most common feature of all those methods is homogenisation or averaging in one or another form. The information from smaller scales (Fig. 2.3, left) and the governing operator $\mathcal{M}$ is homogenised to yield an average effective operator $\mathcal{A}$ acting on average fields, defined in large-scale domain (Fig. 2.3, right). If there are more than two separate scales present, then this process can be repeated for the next scale.

An excellent review categorising all available approaches has been done by Scheibe *et al.* (2015). They propose a multi-scale analysis platform (MAP) flow-chart, which guides readers through different questions and leads to a specific "motif". Within each motif they describe a particular version of a multi-scale method which should be useful, and provide references for further information. In this work we focus on method, in which different scales are decoupled completely. The reason for the decoupling is the small Reynolds number creeping flow in poroelastic material, which can be described by the linear Stokes equations. Such a method would fall within "motif B" in the MAP. As referenced
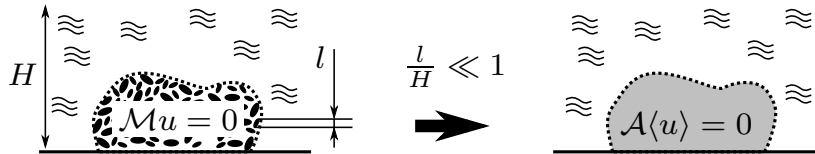
FIGURE 2.3. An example of a homogenisation process. On left, we show a fine-scale porous structure (with characteristic pore size l) in a free-fluid (with characteristic scale H). On the right, we show a homogenised description of the same porous structure containing only average variables. This approach is valid if scale separation exists $l/H \ll 1$.

in the MAP, review of such methods with applications to hydrology is done by Cushman *et al.* (2002). The authors have investigated a number of multi-scale methods, ranging from the method of volume averaging to the random walk method. At the end of the review, a subjective categorisation of such methods is presented. According to Cushman *et al.* (2002), for micro-structure geometries, which are deterministic periodic (based on multiplying the same structure over and over again), volume averaging by Whitaker (1998) or homogenisation via multi-scale expansion, as, for example, explained by Mei & Vernescu (2010), could be useful.

We compare two methods suitable for deterministic periodic microsctructures and analyse the operations that has to be carried out. Both volume averaging by Whitaker (1998) and homogenisation by Mei & Vernescu (2010) make use of (i) the scale separation; (ii) averaging procedure; and (iii) expansion. Therefore we conclude that the two methods are rather similar. The only difference between the methods is the order of sequence at which these operations are carried out. In the method of volume averaging, one first carries out the averaging operation, then uses Gray's decomposition to get equations for the deviations, and finally uses scale separation and locality assumption to create and the solve closure problems. On the other hand, in the method of homogenisation one starts with the scale separation, then renders the governing equations non-dimensional using appropriate scale assumptions on the quantities, expands the equations to obtain the closure problems, and finally averages (homogenises) the solution. Summary of the main steps is given in Fig. 2.4.

More detailed in-depth comparison between these two techniques is performed by Davit *et al.* (2013). In their work, all the steps and assumptions of each method are thoroughly scrutinised. At the end of their work (Davit *et al.* 2013, Fig. 12) a subjective spider-web diagram is presented, comparing these two methods with respect to various criteria. In particular, they state that the method of volume averaging is easier to use on a new case compared to homogenisation, while the roles should be changed for a known case. This conclusion is, of course, subjective. In our experience with working on both
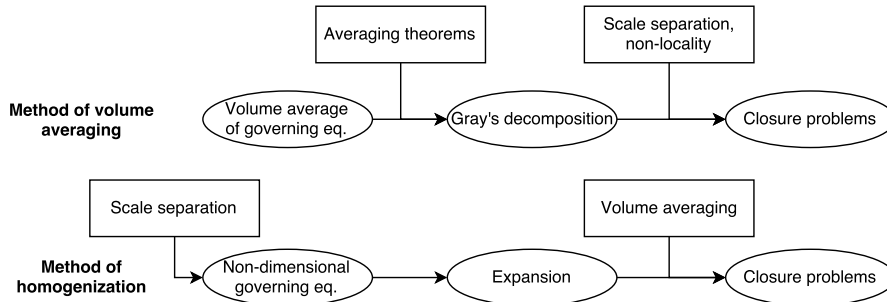
FIGURE 2.4. Flow chart of key elements in the method of volume averaging (top) and the method of homogenisation via multi-scale expansion (bottom).

of these methods, application to known case is equally easy (or difficult) using both of these methods, however, applying those methods to unknown case for us (boundary conditions and elasticity) showed that it was easier to use method of homogenisation via multi-scale expansion. Nevertheless, we acknowledge that both of these methods have their own strengths and weaknesses. While in the current thesis we have worked only with homogenisation via multi-scale expansion in depth, it seems that for the best results, both methods should be used concurrently.

We compare the basic ingredients of methods of volume averaging and homogenization, which has to be used in order to arrive with an averaged / homogenised description of a multi-scale problem. In the method of volume averaging (Whitaker 1998), the governing equations are averaged over a characteristic volume V as a first step. The superficial average of a given variable ψ_α of a phase α (fluid f or solid s) is defined as

$$\langle \psi_\alpha \rangle \equiv \frac{1}{V} \int_{V_\alpha} \psi_\alpha \, \mathrm{d}V = \varepsilon_\alpha \langle \psi_\alpha \rangle^\alpha, \qquad (2.7)$$

where V_α is the volume occupied by the phase α, $\varepsilon_\alpha = V_\alpha/V$ is the volume fraction of phase α and $\langle \psi_\alpha \rangle^\alpha$ is the intrinsic average of the same variable. The core of the method is the spatial averaging theorem

$$\langle \boldsymbol{\nabla} \psi_\alpha \rangle = \boldsymbol{\nabla} \langle \psi_\alpha \rangle + \int_{A_{fs}} \psi_\alpha \hat{n}_{fs} \, \mathrm{d}A, \qquad (2.8)$$

where A_{fs} is the interface between the fluid and the solid, and $\hat{n}_{fs}$ is the normal vector pointing into the solid phase. Another fundamental definition is the transport theorem,

$$\left\langle \frac{\partial \psi_\alpha}{\partial t} \right\rangle = \frac{\partial \langle \psi_\alpha \rangle}{\partial t} - \int_{A_{fs}} \psi_\alpha \mathbf{w} \cdot \hat{n}_{fs} \, \mathrm{d}A, \qquad (2.9)$$

where $\mathbf{w}$ is the local velocity of the interface, which in a fluid-solid system is equal to the local value of the solid boundary velocity. The variables in integrals

arising from both of these theorems are expanded using Gray's decomposition

$$\psi_\alpha = \langle \psi_\alpha \rangle^\alpha + \tilde{\psi}_\alpha, \tag{2.10}$$

where $\tilde{\psi}_\alpha$ is the deviation of the variable. The deviation terms often need to be solved for using an appropriate closure problem (Whitaker 1998). The volume-averaged formulations for the Navier-Stokes equations in a porous case are relatively well-established. The averaging has been extensively explained by Whitaker (Whitaker 1986a, 1996, 1998) and later used by Hussong et $al.$ (2011). However, the treatment of the elasticity and the boundary conditions has not reached the same level of maturity, or is mostly theoretical. Boundary conditions between porous material and free fluid has been proposed by Ochoa-Tapia & Whitaker (1995), and later re-derived by Minale (2014b), who put additional effort into describing how the stress is partitioned between solid and fluid part of the poroelastic material. Nevertheless, Minale (2014b) does not provide practical solutions to the closure problems.

The homogenisation via multi-scale expansion, on the other hand, starts by introducing fast and slow coordinates $x = \tilde{x}/l$ and $X = \tilde{x}/H$, respectively. The tilde denotes dimensional coordinate. Any variable is then expanded in the form of a power series and generalised to the new function arguments, which in the one-dimensional time dependent setting is

$$\psi(x,t) \quad \rightarrow \quad \psi(X,x,t) = \psi^0 + \epsilon\psi^1 + \epsilon^2\psi^2 + \ldots, \tag{2.11}$$

where the variables ψ^k $(k = 0,1,2,\ldots)$ are functions of the arguments X, x and t. It is important to note that the variable in question is extended from a one-dimensional space to a two-dimensional space, as illustrated in Fig. 2.5. However the two-dimensional formulation is arbitrary up to the slice, defined by the scaling $X = \epsilon x$. The spatial derivative is given as

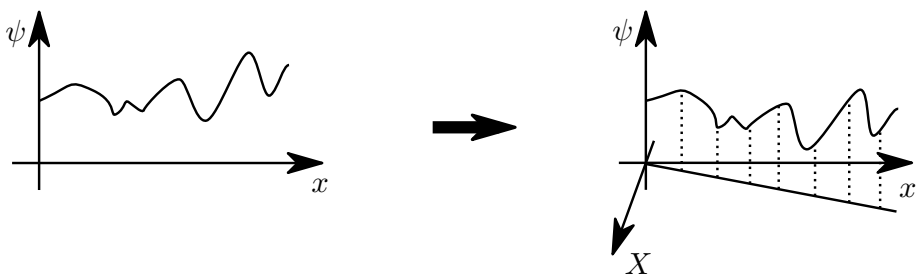$$(\cdot)_{,i} = (\cdot)_{,i_1} + \epsilon(\cdot)_{,i_0}, \tag{2.12}$$

FIGURE 2.5. The starting point of the multi-scale expansion technique is the generalisation of a quantity, which is a function of one physical coordinate (x), into another quantity, which is a function of two coordinates (a micro-scale x and a macro-scale X).

where we have used comma to denote differentiation. The term $(\cdot)_{,i}$ denotes derivative with respect to the original coordinate; the term $(\cdot)_{,i_1}$ is derivative with respect to the micro-scale coordinate x; and the term $(\cdot)_{,i_0}$ is the derivative with respect to the macro-scale coordinate X. After applying the expansion both in amplitude and in coordinate space, one arrives with governing equations at different orders. These equations then have to be solved one-by-one in micro-scale. After the solution is obtained in micro-scale, the results can be averaged and used in effective equations.

In order to give an example of volume averaging and homogenization methods, we briefly illustrate equations, which can be obtained by starting from Navier-Stokes equations in pore-scale (2.1–2.3). Applying the volume averaging (Whitaker 1998) on the governing equations (allowing the solid skeleton to be elastic) leads to

$$\rho \left[\frac{\partial \langle \mathbf{u} \rangle^f}{\partial t} + \left(\langle \mathbf{u} \rangle^f \cdot \boldsymbol{\nabla} \right) \langle \mathbf{u} \rangle^f \right] = -\boldsymbol{\nabla} \langle p \rangle^f + \mu \nabla^2 \langle \mathbf{u} \rangle^f + \mathbf{f}_1, \qquad (2.13)$$

$$\boldsymbol{\nabla} \cdot \langle \mathbf{u} \rangle^f = \mathbf{f}_2, \qquad (2.14)$$

where $\langle \cdot \rangle^f$ is an intrinsic average of the flow and pressure fields, as defined before. The obtained equations are similar to the pore-scale Navier-Stokes equations (2.1–2.3) except for two source terms. The source term in the momentum equation $\mathbf{f}_1$ contains the viscous dissipation due to the creeping flow and other pore-scale effects, and the source term in the continuity equation $\mathbf{f}_2$ describe the source or the sink of the averaged velocity field arising from the change of fluid volume fraction in the medium. These equations are employed by Hussong *et al.* (2011) to describe flow fields caused by beating cilia. In order to recover the classical Darcy's law with or without Brinkmann's correction, additional assumptions connected to scale separation must be employed to neglect the inertial (and the viscous) terms in the averaged setting (Whitaker 1996). On the other hand, in the method of homogenisation via multi-scale expansion by Mei & Vernescu (2010), one immediately uses the scale separation on the pore-scale Navier-Stokes equations, and at the first order directly obtains the relative Darcy's law

$$\langle \mathbf{u} \rangle^f - \partial_t \langle \mathbf{v} \rangle^f = -\frac{\mathbf{K}}{\mu} \cdot \boldsymbol{\nabla} \langle p \rangle^f, \qquad (2.15)$$

$$\boldsymbol{\nabla} \cdot \langle \mathbf{u} \rangle^f = \mathbf{f}_2, \qquad (2.16)$$

where $\partial_t \langle \mathbf{v} \rangle^f$ is the averaged velocity of the solid phase and $\mathbf{K}$ is a permeability tensor. Using this approach it is quicker to obtain the Darcy's law directly, while adding the Brinkmann correction (Auriault *et al.* 2005) or the inertial terms (to the best of author's knowledge, this has not been done using homogenization via multi-scale expansion) requires seemingly much more work compared to the method of volume averaging.

2.2. Numerical simulations

After having settled on the theoretical model that accurately describe a system in question and after obtaining corresponding governing equations, numerical experiments can be employed. The equations must be discretised using a numerical scheme. The possible choices are vast. A large group of numerical tools use finite volume methods (FVM), which are easy to understand, therefore very widely used by engineers. In FVM, the governing equations are re-written in an integral form around some control volume, and then the integral form is evaluated numerically. For more information, see the book by Moukalled *et al.* (2015). Another group of simple discretisations, which is also the oldest numerical method, is the finite difference methods (FDM). In FDM, the original form of point-wise continuous partial differential equation is used and each derivative is approximated using a given support stencil, which consists of a few discrete points in space and time. The reader can find FDM formulas for grids with arbitrary spacing in the work by Fornberg (1988). However, the boundary condition treatment is relatively cumbersome due to required modification of the differentiation stencils. The last and most theoretically involved group of simulation methods is the finite element methods (FEM). The FEM is according to opinion of many researchers most elegant in terms of mathematical treatment. For the FEM, one has to define an appropriate test function space, and then multiply the governing equations with the corresponding test function. The equations are then integrated over the whole domain and a weak formulation is derived. In such way, an approximation of the real solution, which has the smallest error in the defined function space, is found. For fluid flow simulations, FEM with spectral basis is gaining popularity due to high accuracy and good scaling properties on parallel computers. For the theory of spectral element methods (SEM), the reader is referred to the book by Karniadakis & Sherwin (2013). Another good reading material on various numerical methods applied for numerical solutions of flow models is the book by Ferziger & Perić (2002).

Regardless of the chosen method, the next step is discretisation of the physical domain using a mesh (or other numerical representation for mesh-free methods). The standard way to achieve this, is using body-fitted mesh, i.e., mesh, which is conforming to the body. Except for very few specific shapes of the body (such as squares or rectangles), the body fitted mesh approach is rather complex. The easiest is to generate an unstructured mesh, which does not contain any underlying global structure. An example of body-fitted unstructured triangle mesh is shown in Fig. 2.6 (left). Such a mesh is typical for numerical simulations with FEM, and can also be used with FVM. In this work, we use the FEM with body-fitted mesh for simulations with FreeFem++ (Hecht 2012), which is a convenient toolbox to test different physical models and boundary conditions. For FVM and FDM, however, the domain is typically discretised using a structured mesh, which has a global structure. The simplest possible structured mesh is a uniform mesh, as shown in Fig. 2.6 (right). The
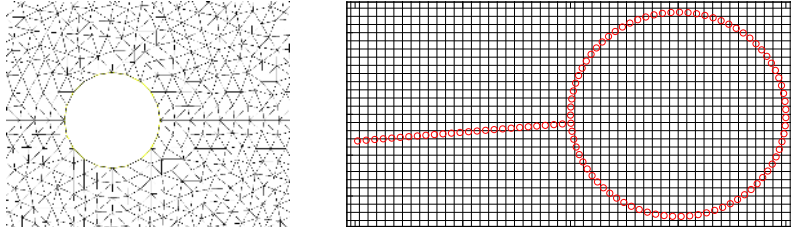
FIGURE 2.6. Example of two meshes used for numerical simulations. On the left, we show a body fitted triangular unstructured mesh around a cylinder. On the right, we show a uniform quadratic structured Eulerian mesh around cylinder with splitter plate within a IB framework, in which the body is represented using a separate Lagrangian grid (red circles).

FVM and FDM on such discretisations can be very efficient due to application of fast Fourier solvers (for periodic conditions).

If one would like to carry out numerical simulations of moving bodies, then the standard approach with body-fitted mesh (Fig. 2.6, left) is computationally expensive due to the requirement of a changing mesh, which has to be either deformed or re-created. In order to avoid this difficulty, a so called immersed boundary (IB) method can be used, which we also employ in part of this work. The IB method was originally developed by Peskin (1972) for describing flow patterns around heart valves. The underlying idea is to discretise the Navier-Stokes equations on a regular structured grid (Eulerian mesh in Fig. 2.6, right), and represent a body of arbitrary geometry on a separate grid (Lagrangian mesh in Fig. 2.6, right), which can move freely with respect to the fluid grid.

The interaction between the Lagrangian and the Eulerian grids is imposed by interpolation and spreading (regularisation) operators. The velocity of the fluid $\mathbf{u}(\mathbf{r})$ is interpolated from the Eulerian grid to the Lagrangian grid, while the forcing from the solid body $\mathbf{F}(\mathcal{L})$ is spread from the Lagrangian to the Eulerian grid

$$\mathbf{U}(\mathcal{L}) = \int_{\Omega} \mathbf{u}(\mathbf{r}) \, \delta(\mathbf{r} - \mathcal{L}) \, \mathrm{d}V, \tag{2.17}$$

$$\mathbf{f}(\mathbf{r}) = \int_{S} \mathbf{F}(\mathcal{L}) \, \delta(\mathcal{L} - \mathbf{r}) \, \mathrm{d}S. \tag{2.18}$$

Here, $\mathbf{r}$ is the coordinate vector from the origin of the coordinate system to any point on the Eulerian grid, $\mathcal{L}$ is the coordinate vector from the origin of the coordinate system to any point on the Lagrangian grid, $\mathbf{U}(\mathcal{L})$ is the interpolated velocity on Lagrangian points, $\mathbf{f}(\mathbf{r})$ is the regularised force density on the Eulerian points, and $\delta(\mathbf{r} - \mathcal{L})$ is the regularised Dirac delta function. The main advantage of IB methods is their efficiency, because the simplicity of the structured fluid mesh is preserved and there is no need for deforming or re-creating the fluid mesh. On the other hand, one has to deal with inaccuracies

introduced by interpolation and spreading operations, as well as with a fictitious fluid inside the body.

All numerical simulations contains errors. The most common one is the discretisation error; that is, error, which is caused due to the representation of a continuum model in a discrete way. It includes both spatial disctretisation error (connected to mesh size) and temporal discretisation error (connected to time step). The numerical simulations of turbulent flows are very prone to these errors, because the structure of the flow is very complex, containing small and large scale entities. Less common is the modelling error; that is, an error, which is caused due to an insufficiently accurate continuum model for the specific problem. For example, the incompressible Navier-Stokes equations are not able to capture the flow behaviour close to the speed of sound and rise of shock waves. In order to be confident about the problem description using numerical simulations, one always has to check the discretisation error and also think about modelling error.

2.3. Experiments

While theoretical approaches and numerical simulations are often practically cheap, provide detailed results, which are not always accessible from experiments, experimental investigations have been and always will be an invaluable asset in scientific ventures. The reason is the fact that the real-life experiments are fully governed by fundamental laws in nature, while numerical simulations and theoretical efforts must always be based on mathematical models. To be fair, one has to note that experiments alone would also be useless, because without theoretical models, one could not understand the measurement devices. Although this statement is strong, one has to remember that even the most well founded and the most widely accepted theory still is a required ingredient for the measurements. For example, the commonly used Pitot or Prandtl tubes has been designed based on the Bernoulli's law. Without the theory, the measurement would not have any interpretation. Empirical and heuristic models can also be viewed as the simplest possible theoretical description. To sum up, theoretical, numerical and experimental efforts should be used hand-in-hand in order to achieve scientific progress.

There are many types of experimental facilities and measurement methods used for experiments on flows and solids. To give a few examples, very wide spread experimental tools in fluid mechanics are wind tunnels (example shown in Fig. 2.7a), water tanks and water tables. The flow field can be visualised using dye or smoke (Fig. 2.7a), but for more quantitative observations one has to use more sophisticated techniques, such as particle-image-velocimetry (PIV) and laser-Doppler-velocitmetry (LDV) for flow field investigations, or pressure tubes and hot-wire anemometry for flow velocity investigations in a particular point. For experiments with solid structures measurement techniques are required, which are able to resolve also the solid displacement, as, for example, can be done using optical coherence tomography (OCT).
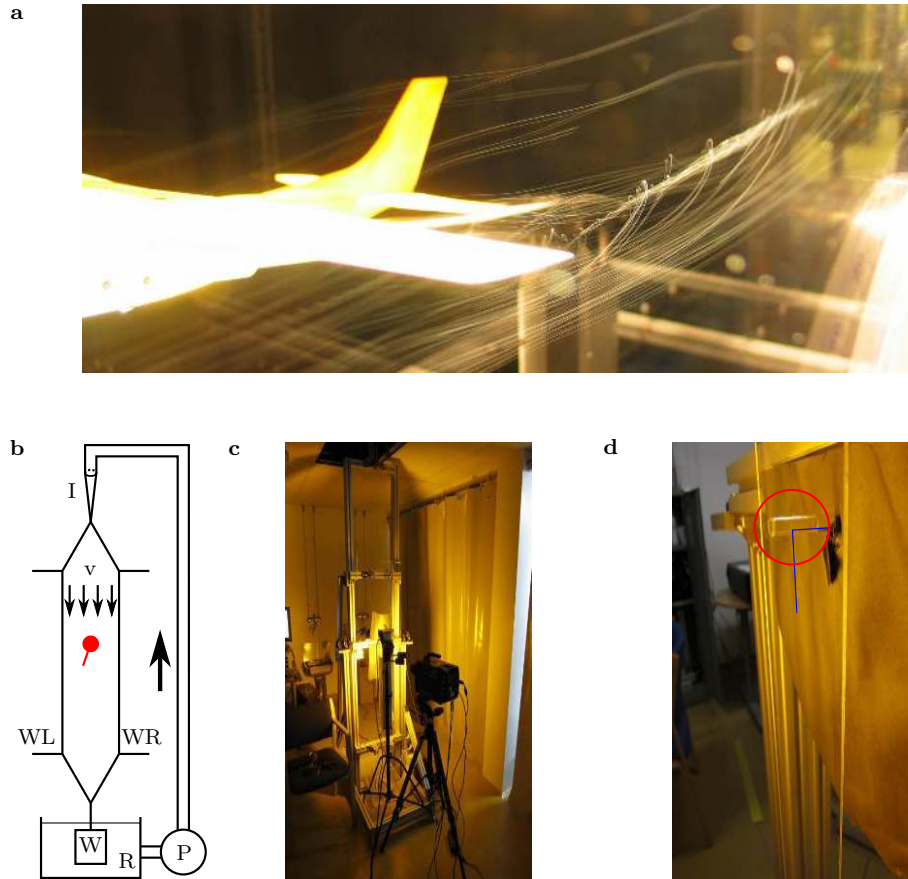
FIGURE 2.7. Example of a wind tunnel experiment (a) in RPI Subsonic Wind Tunnel, where a model of Cessna 182 is tested. A wingtip vortex is visualised using smoke. Photo by Dale (2007). Schematic of a soap-film experimental facility (b). Overview of experimental facility in Stockholm (c), and zoomed view of a cylinder (indicated with a red circle) with a filament (indicated using a blue line) immersed inside the soap-film (d).

It is possible also to carry out two-dimensional (2D) experiments. As surprising as it may be, there are 2D flows present also in nature, most notable example is the large scale atmospheric and ocean flow, which is globally 2D due to stratification (difference in fluid density). Smaller scale experiments in 2D can be carried out using a soap-film apparatus. Since the work by Couder (1984); Couder *et al.* (1989) and Kellay *et al.* (1995) on turbulence in a soap-film, this experimental method have been developed tremendously and has

found applications in FSI field as well. The soap-film experiment is widely known as a good approximation to a two-dimensional experiment and as such it is suitable to compare with our two-dimensional numerical simulations. A schematic of a soap-film apparatus is shown in Figure 2.7b. We have built our own apparatus with feedback from Prof. Kellay (Bordeaux), the pictures are shown in Figure 2.7c,d.

The soap solution is driven from the reservoir by a pump P (Figure 2.7b) to the top. Then soap solution falls between two nylon wires under the influence of gravity and forms a thin soap-film. The film flows around an object placed in the test section (fixed or free to rotate), thus forming a wake behind the body. The thickness variations of the soap-film serve as a proxy of the vortex structures in the flow field. The measurements of the flow field can be done using a high-speed camera or LDV system.

The experiments are not influenced by the errors, which would appear in numerical simulations – the fundamental laws of nature are always present and there are no discretisation errors. However, the experiment must be carried out using measurement devices. And the results obtained from the experiments are also prone to two types of errors; the first being random error and most often caused by the accuracy of the measurement device; the second being systematic error and most often caused by the influence from the measurement device on the experiment itself. The main challenge in matching the experimental measurements with numerical simulations is to have sufficient control over all errors, such that one can, with good enough confidence, state that the investigated problem is the same from both (experimental and numerical) sides. In this thesis I further focus on numerical and theoretical efforts, but corresponding experimental results, where applicable, can be found in the papers in the second part of this thesis.

CHAPTER 3

Individual appendage in a flow

In this chapter, we give an overview of our work towards understanding, how a single appendage behind a bluff body behaves, if the body is moving or is exposed to an incoming flow stream, which is the first objective outlined in section 1.2. The starting point for this work is the symmetry breaking for an elastic filament behind a cylinder, as reported by Bagheri *et al.* (2012), and also symmetry breaking of a system consisting of a cylinder with a splitter plate clamped at the rear end, as analysed by Xu *et al.* (1990) and Cimbala & Chen (1994). We investigate a single appendage behind an object freely falling under the influence of gravity to understand if any favourable behaviour is triggered by the previously reported symmetry breaking.

3.1. Numerical investigations

We use the IB projection method developed by Taira & Colonius (2007), which is an extension of fractional-step FVM originally introduced by Perot (1993). To carry out simulations, we have proposed additional modification of the method to include the rigid body motion solver implicitly (Lācis *et al.* 2016, paper 2). By doing so, we are able to investigate freely falling bodies with density ratio between the body and the surrounding fluid close to unity.

We define the fluid domain Ω_f as a rectangular box, shown in Fig. 3.1, left. The domain is meshed using a structured rectangular mesh, with a grid that is uniform in the region of movement and expanding towards the sides of the boundary. The requirement of uniform mesh spacing arise from the discrete Dirac delta function, used to couple the solid body boundary $\partial\Omega_{fs}$ with the fluid mesh. The gravitational acceleration is pointed towards the bottom of the domain. At the outer boundary of fluid region $\partial\Omega_{fo}$, we impose no-slip boundary condition.

From the simulations, we conclude that the cylinder with the splitter plate after some initial transient turns and drifts towards left or right. The direction of the drift is determined by the initial condition. In Fig. 3.1, right, we show a snapshot of a steady drift obtained for Reynolds number $Re = 156$. We have identified that the body turns by an angle $\theta = 19°$ with respect to the direction of motion, and the drift angle is $\alpha = 8°$ with respect to the direction of gravity. For more results in the two-dimensional setting and experiments on soap-film, see paper 1 (Lācis *et al.* 2014).
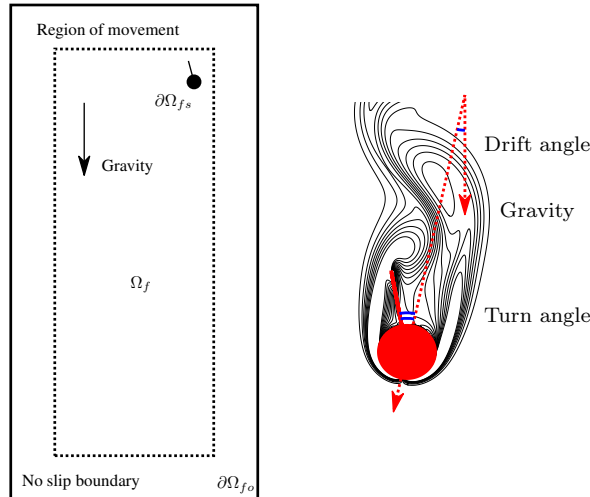
FIGURE 3.1. Set-up of numerical simulations, used to investigate a freely falling cylinder with a splitter plate clamped at the rear. On the left, we show a simulation domain, with the region of the uniform mesh identified using dashed lines. Boundary condition at all of the sides of the box is zero velocity, and the fluid inside the box is at rest. On the right, we show a snapshot of simulation at Reynolds number 156 and identify the direction of gravity and body motion, as well as turn angle and drift angle.

As indicated by Lācis *et al.* (2014), such an instability is also present in three dimensions. To carry out further investigations in three dimensions, we select an elliptic shape of appendage behind a sphere and carry out numerical investigations for different aspect ratios A and lengths L of the appendage. In order to simplify the numerical task, it is assumed that a reasonable approximation of the behaviour exhibited by the freely falling body can be obtained by steady, fixed body simulations. This assumption is reasonable for Reynolds number $Re = 200$ which renders the wake of the sphere steady. An illustration of the sphere with the elliptic appendage placed in the free-stream undergoing the same symmetry breaking as the cylinder with the splitter plate is shown in Fig. 3.2a. Two stream-wise velocity iso-surfaces behind the sphere with an appendage of aspect ratio $A = 0.7$, length $L = 0.7 D$ and turn angle $\theta = -11.3°$ are shown in Fig. 3.2b. From the figure, we observe that there is a relatively large back flow region at one side of the elliptic appendage, while it does not exist on the other side of the appendage. We have then varied the aspect ratio and length of the appendage in order to seek the optimal shape of the appendage, which generates the largest lift force. For more results and discussion, see paper 3.
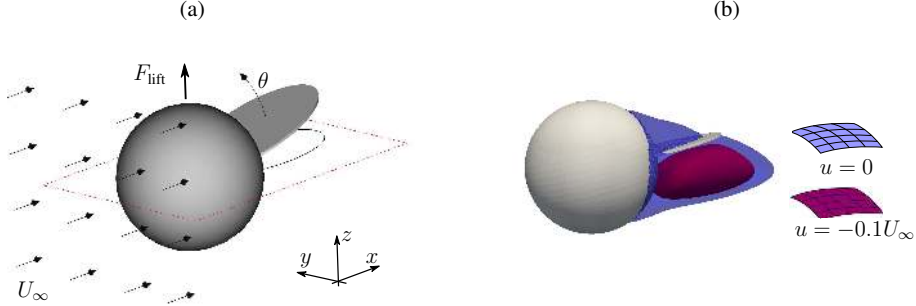
FIGURE 3.2. Sphere with an appendage shaped like an ellipse placed in a free stream of velocity U_∞ is shown in panel (a). The sphere has a diameter D and the appendage has a length L. Due to symmetry breaking, a turn by an angle θ as well as a lift force F_lift is generated. In panel (b) we show iso-surfaces of two stream-wise velocity values $u = 0$ (blue) and $u = -0.1\,U_\infty$ (red). The turn angle of the body is $\theta = -11.3°$. Length of the elliptic appendage is $L = 0.7\,D$ and the aspect ratio is $A = 0.7$.

It turns out that this instability both for two-dimensional and three-dimensional bodies is the same one as previously observed by Xu *et al.* (1990); Cimbala & Chen (1994); Bagheri *et al.* (2012), but up till now the exact mechanism was not uncovered. In the following sections, we briefly describe the main reason for this symmetry breaking and also possible consequences.

3.2. Inverted-pendulum-like instability

In this section, we summarise a simple mathematical model, which we have proposed as an explanation for the observed symmetry breaking. The model is based on an intuitive mechanical system, namely the inverted pendulum. Therefore, we call this the inverted-pendulum-like (IPL) instability. Consider an inverted pendulum, which consists of a cylinder and a plate attached to it, as shown in Fig. 3.3a. The pendulum is anchored at the center of mass of the cylinder; the center of mass of the whole body is located slightly above the attachment point. There are solid walls at the sides of the system. The straight upright position of the pendulum is an equilibrium state, however, it is unstable. That is, if there is any disturbance in the system, the pendulum would fall, either to the left or to the right, depending on the disturbance.

We suggest that the cylinder with the splitter plate freely falling in fluid or exposed to incoming free stream is a similar system. The role of the gravitational forces are played by pressure forces in the back flow region (Fig. 3.3b), which essentially try to push the spitter plate out of the back flow region, given that the plate is sufficiently short. On the other hand, the forward flow is playing the role of side walls, providing with counter-acting force. This sets a
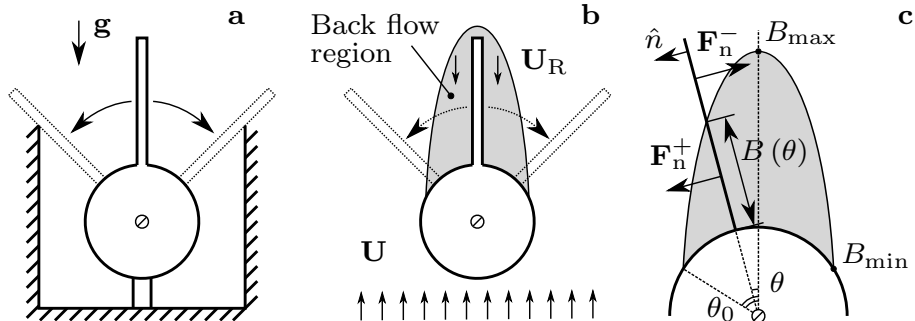
FIGURE 3.3. Illustration of the model, which we propose as explanation for the observed fluid-structure-interaction symmetry breaking. In frame (a), we show a system of the unstable inverted pendulum, which is encompassed by walls at both sides. In frame (b), we sketch a splitter plate, which is fully enclosed in a back flow region, created due to presence of the cylinder. In frame (c), we show a force balance at an equilibrium angle θ between forces from the back flow and forward flow.

unique turn angle, at which the total torque caused by the plate around the center of the cylinder is zero.

In order to obtain more quantitative predictions, we have devised a simple model of two forces acting on the two different parts of the splitter plate. First, we assume that the splitter plate is infinitely thin, such that any thickness effects can be neglected. We define the normal direction $\hat{n}$ on the plate as shown in Fig. 3.3c.

We define two normal forces acting on the plate. One is the force driving the instability, i.e., trying to turn the plate away from the center, and is defined as

$$F_n^+ = 2k \sin(\theta) A \rho_f U^2 B(\theta).$$ (3.1)

Here, $B(\theta)$ is the length of the splitter plate located inside the back flow region, or in other words, length of the plate exposed to normal force in the "plus" direction. The second is the stabilisation force, i.e., trying to oppose the instability, and is defined as

$$F_n^- = 2 \sin(\theta) A \rho_f U^2 [L - B(\theta)].$$ (3.2)

Here, $L - B(\theta)$ is the length of the splitter plate located outside of the back flow region and is exposed to normal force in "minus" direction. The constants k and A are force model calibration constants; the parameter k shows the relative magnitude of force inside the back flow region compared to force outside of the back flow region, and parameter A characterises the magnitude of both forces. After determining the forces acting on the splitter plate, one can construct the corresponding torque around the center of the cylinder. In the IPL model it is
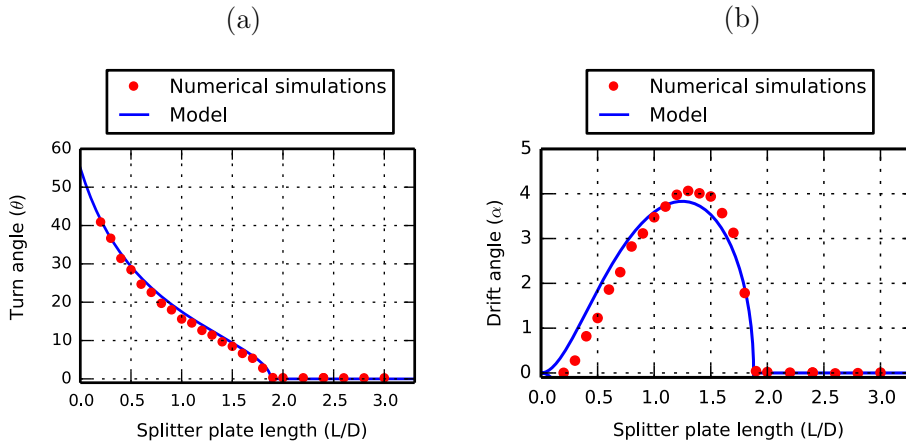
(a)   (b)

FIGURE 3.4. Results of the inverted-pendulum-like model compared with direct numerical simulations for a freely falling cylinder with splitter plate. The solid density ratio is $\rho_s/\rho_f = 1.001$ and the Reynolds number is $Re = 45$. In frame (a), we show the turn angle with respect to splitter plate length. In frame (b), we show the drift angle for same splitter plate lengths.

assumed that equilibrium solutions are the ones with zero torque arising from the forces on the splitter plate.

We choose the model calibration constants by comparing the model predictions with observables from the numerical simulations. Then we compare the model predictions with direct numerical simulations of a freely falling cylinder with a splitter plate of different lengths. The density ratio is $\rho_s/\rho_f = 1.001$ and the Reynolds number is $Re = 45$. Turn angle results are given in Fig. 3.4a. The model has been successful in predicting the drift angle of the freely falling body. The forces acting on the plate can be projected in normal direction to the incoming free stream and thus obtain the side force on the body. Since the level arm for the force towards left ($\mathbf{F}_n^+$) is smaller compared to the level arm for the force towards right ($\mathbf{F}_n^-$, Fig. 3.3c), the force towards left must be larger than the force towards right. Therefore, the drift is towards the direction, in which the plate is tilted, as seen in Fig. 3.1b. More quantitative comparison of obtained drift angles for different splitter plate lengths is shown in Fig. 3.4b.

Additional discussion about the model validation and quantitative comparison with soap-film experiments can be found in paper 1 (Lācis $et\ al.$ 2014), and corresponding supplementary material.

3.3. Effects of elasticity

In this section, we describe additional effects of elasticity on the IPL instability. Experimental investigations of a three dimensional system consisting of a

cylinder with an attached elastic filament has been carried out by Brosse *et al.* (2015). They found that if the filament is shorter than some critical length, it collapses near the surface of the cylinder. This effect has been attributed to both the IPL and also buckling instability – collapse of a filament structure by bending under load aligned with the filament.

Our study is carried out in a two-dimensional setting. We replace the rigid splitter plate of the freely falling cylinder with a deformable one-dimensional filament, similar to the one used by Bagheri *et al.* (2012). The difference between the set-ups is that in the reference paper (Bagheri *et al.* 2012) the filament is hinged to the cylinder (filament can freely change angle with respect to cylinder surface) and the cylinder can not rotate, while in this work the filament is clamped to the cylinder (the angle between filament and cylinder close to the attachment point is always 90°) but the cylinder itself can rotate. Illustration of the proposed system is shown in Fig. 3.5a. For the purpose of the numerical simulation, filament is assumed to be infinitely thin, inextensible and massless.

In order to carry out numerical simulations, we complement the developed numerical method (Lācis *et al.* 2016, paper 2) with an explicit solver for the one dimensional elastic beam, as employed by Bagheri *et al.* (2012). Due to the explicit nature of the elastic solver, the time-step restriction on the numerical simulations was much stricter compared to rigid body solver only. Therefore, we were only capable to carry out investigations of the elastic appendages for a limited time in the free fall regime.
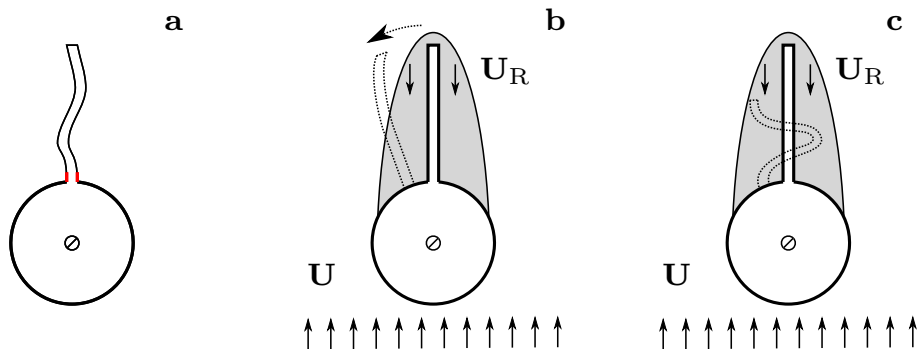

FIGURE 3.5. Illustration of the body, which consists of a cylinder and an elastic filament clamped (denoted with red) at the rear end, frame (a). In frame (b), we sketch one possible behaviour of the system, in which the filament undergoes the same IPL instability as the rigid plate, but there is a visible deformation. In frame (c), we sketch another possible behaviour, in which the filament undergoes a buckling instability in addition to the IPL instability.
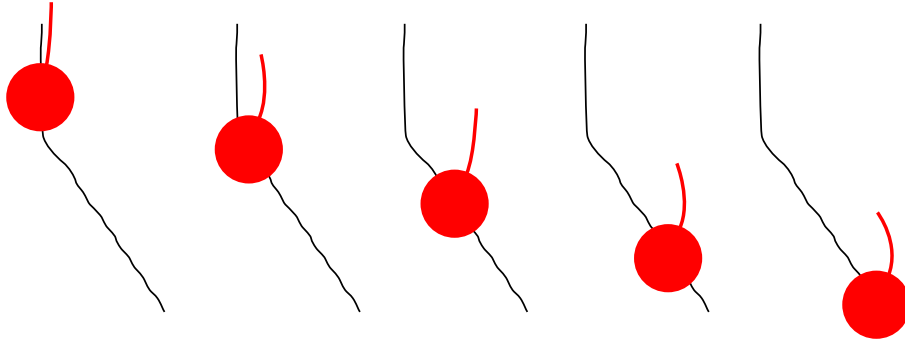
FIGURE 3.6. Results of freely falling cylinder with elastic filament clamped behind it. The length of the filament is $L = 1.0\,D$. The body is shown at five different time instances. The free-fall trajectory is shown by the black line, which is not in scale with the body.
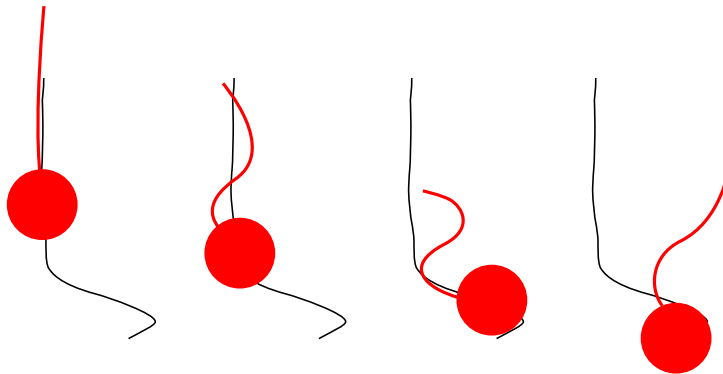

FIGURE 3.7. Results of freely falling cylinder with elastic filament clamped behind it. The length of the filament is $L = 2.4\,D$. The body is shown at five different time instances. The free-fall trajectory is shown by the black line, which is not in scale with the body.

We carry out simulations of a freely falling cylinder with a soft elastic appendage of length $L = 1.0$. The body with filament shape at five different time instances is shown in Fig. 3.6. We also show the trajectory of the falling body in black (not in scale with the body). From this figure, one observes a very similar behaviour to that with a rigid plate – the body turns and drifts towards one side. The only signature of the elasticity is the slightly deformed shape of the filament. This behaviour can be explained exactly in the same way as the IPL instability and is illustrated in Fig. 3.5b.

We repeat the simulation for longer $L = 2.4\,D$ and softer filament (with 40% smaller bending coefficient). The trajectory and body shapes at four distinct time moments are shown in Fig. 3.7. From this figure, we conclude that in addition to the IPL instability, the filament also buckles. After the buckling, the body turns again, same as for the IPL instability. However, it drifts to the opposite direction. Although this symmetry breaking is very different from that of an IPL instability, we believe that the cause is very similar. That is, due to the back flow region behind the cylinder, the filament buckles, if the combination of filament length and bending rigidity is permitting it. We have sketched this behaviour in Fig. 3.5c.

These numerical simulations, which we were able to carry out only in the transient free fall regime, are giving an indication of what one could expect if the elasticity is coupled with the IPL instability. For some parameter range the results would remain largely the same as for the rigid case. However, for other parameter combinations, an elastic instability – buckling – appears, which has a large effect on the freely falling motion. In order to fully characterise the effect of elasticity in the future, longer simulations would be required that would reach a steady free fall regime, if there exists one. In addition, the numerical method development should be continued with the objective to reduce the numerical cost of such simulations. A possible direction would be to implement elastic filament treatment implicitly, similarly as done for hte vorticity-based IB method by Wang & Eldredge (2015).
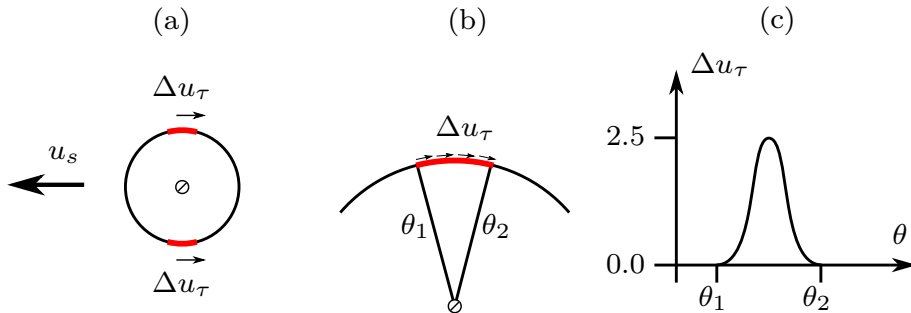

FIGURE 3.8. Illustration of swimming cylinder model. In frame (a), we show two regions at the surface of the cylinder, where velocity difference of tangential velocity Δu_τ is imposed between the solid body motion u_s and the surrounding fluid motion. In frame (b), we illustrate this velocity difference or jet production in zoomed view. In frame (c), we show velocity difference as a Gaussian function, which we use to match the boundary condition continuously with the no-slip condition.

3.4. Swimming-like motion

We also investigate the IPL instability for swimming bodies. To that end, we take advantage of the developed numerical method (Lācis *et al.* 2016, paper 2) that allows to prescribe not only no-slip condition between the fluid and the moving rigid body, but also a velocity difference. In order to model a swimming body, we define two segments of the cylinder, located symmetrically at the top and bottom of the cylinder, as shown in Fig. 3.8a. Over these two segments, we impose a tangential velocity difference between the solid body and the surrounding fluid, as illustrated in Fig. 3.8b. A Gaussian function is used, such that the velocity difference at the sides of those two segments is zero, see Fig. 3.8c. At the remaining boundary of the cylinder, we define the no-slip condition. This velocity difference between the solid body and the surrounding fluid acts as a jet and propels the body forwards or backwards, depending on the direction of the jet, as illustrated in Fig. 3.8a.
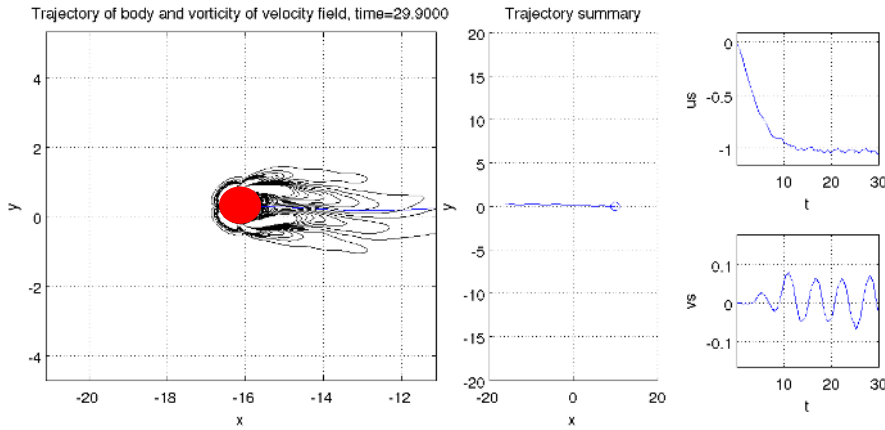

FIGURE 3.9. Results of a cylinder with velocity difference imposed at the top and the bottom, producing a jet that moves it forward. On the left, the vorticity field is shown at the end of the simulation. In the middle, the trajectory line is drawn. On the right, time statistics of the horizontal cylinder velocity u_s and the vertical cylinder velocity v_s are shown.

The maximal value of the velocity difference is set to $\max(\Delta u) = 2.5$. This value was obtained by observing the final velocity of the cylinder alone and matching it to $u_s = 1.0$. The simulation of this problem is carried out in a still fluid. Results from this simulation are shown in Fig. 3.9. The Reynolds number for the simulation is $Re = 40$. In the figure, we have reported the final vorticity field near the cylinder, trajectory curve and also time evolution of the horizontal u_s and the vertical v_s velocity of the cylinder. As expected, due to the produced jets at the sides of the cylinder, the cylinder is moving from the right to the left. After an initial transient, the cylinder reaches an
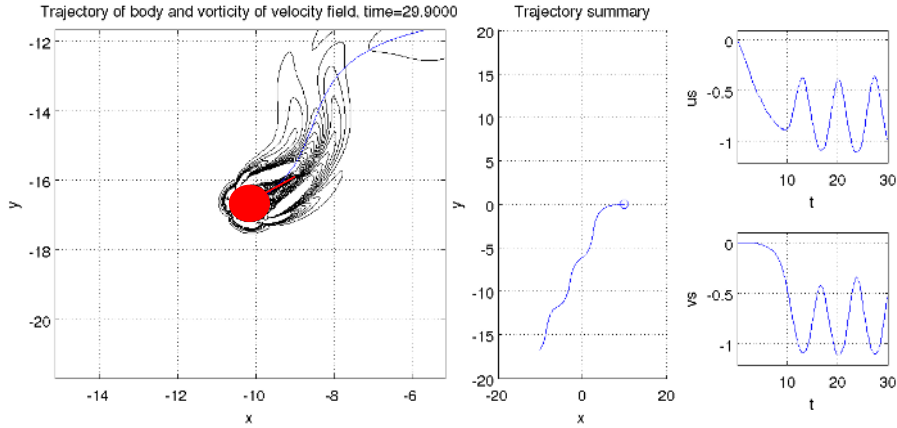
Figure 3.10. Results of a cylinder and a splitter plate with a velocity difference imposed at the top and the bottom of the cylinder, producing a jet that moves the body forward. On the left, the vorticity field is shown at the end of the simulation. In the middle, the trajectory line is drawn. On the right, time statistics of the horizontal cylinder velocity u_s and the vertical cylinder velocity v_s are shown.

approximately constant horizontal velocity $u_s = 1.0$. The vertical velocity is oscillating with roughly zero mean value and an amplitude of around $v_s = 0.05$. Overall, there is no symmetry breaking and the cylinder is moving along a straight path on average. From the vorticity plot at the end of the simulation, one can identify two wakes. The first wake is caused by the jets originating at the sides of the body, and is a propulsion wake. The second wake is caused by the cylinder itself and it is a drag wake.

To trigger the IPL instability, we add a rigid splitter-plate behind the cylinder and drive it using exactly the same parameters at the cylinder sides. The results are presented in Fig. 3.10. Interestingly, after the initial transient, the moving body is translating along the diagonal on average, exhibiting a very wide range of rotation angle. That is, the motion has similarities to that of a fish swimming. It seems that the splitter plate has destabilised the moving body and the generated back flow region is causing oscillations, which resemble a swimming motion.

In the future, to characterise the observed IPL instability effect on swimming-like motion, additional convergence tests and initial condition sensitivity studies need to be performed. Investigations of different plate lengths should be added. Additionally, the IPL model could be applied to this set-up and possibly extended in order to allow for dynamic interaction between the plate and the surrounding propulsion jets.

CHAPTER 4

Poroelastic material in free fluid

In this chapter, we give an overview of our work towards developing a complete mathematical formulation for the free flow problem over porous and poroelastic material, which is the second objective outlined in section 1.2. The direct numerical simulations (DNS) of the governing equations valid at all scales (see sections 2.1.1 and 2.1.2) for multi-scale systems – in which the characteristic size of the pores l is small compared to the macroscopic system size H – are very expensive. This is because there is a very large number of pores in the system, and each pore has to be resolved with a reasonable accuracy. However, the homogenised models contain a lot of assumptions and simplifications. Therefore, the starting point of this work is the DNS of a selected test problem, which we later on use for validation of the continuum model. Then we continue using the homogenisation method via multi-scale expansion (section 2.1.3) to obtain the effective model.

4.1. Direct numerical simulations

Due to the fact that there are many assumptions and simplifications required to formulate a closed multi-scale model, it is desirable that the resulting model is validated. Although the elastic equations derived by Mei & Vernescu (2010) has been known for many years, a detailed validation has not been presented to the best of our knowledge. The most common approach, as employed by Lee & Mei (1997c), is to compute the effective elasticity and validate the resulting tensors with respect to symmetries predicted by anisotropic material theory (Cowin 2013). The closest to what we want to do is the work by Iliev *et al.* (2008), where they have investigated large deformations, that result in non-linear micro-scale problems. They present the theory and then validate the results with DNS. However, up to this day no one-to-one comparison between solution of micro-scale equations (DNS) and a homogenised model of a practical system in two or three-dimensions has been presented.

Therefore, along the way of developing homogenised models, we have set out a task to validate the model as much as possible. For validation, we select a lid-driven cavity problem. When working with porous materials only, two-dimensional systems are sufficient. For validation in the porous case, the bottom of the cavity is filled by regularly spaced cylinders, as shown in Fig. 4.1a. The top wall of the cavity is driven by some velocity U_w, which in turn generates a flow vortex in the cavity. Due to the porous bed, there is a slip velocity
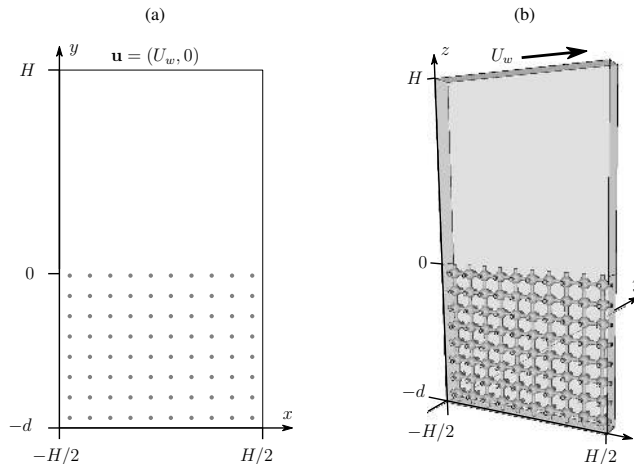
FIGURE 4.1. Lid-driven cavity problem as validation problem for porous material (a) and poroelastic material (b). In the porous case, the bottom of the cavity is filled by discrete cylinders. In the poroelastic case, the bottom of the cavity is filled by spheres in all directions connected using cylinders.

at the interface with the porous region, which appears in the horizontal velocity component, as shown in Fig. 4.2a. Additionally, part of the momentum is transferred through the porous medium via a penetration velocity (vertical velocity component), as shown in Fig. 4.2b. For more details of results, see the paper 4 (Lācis & Bagheri 2016).

For validation in the poroelastic case, we construct a quasi-three-dimensional set-up, as shown in Fig. 4.1b. In this case, the bottom of the cavity is filled with fully-connected three-dimensional structures, which consist of spheres, connected with cylindrical rods in all directions. We consider only one pore-structure in the y direction, extending over the microscale length l. For investigations of poroelasticity, a three-dimensional structure is required. In two-dimensions, all porous materials are disconnected (as cylinders in Fig. 4.1a) and therefore can not transfer stress. On the other hand, all elastic materials, which are connected in all directions and can transfer stress, can contain only isolated pores. That is, no flow through the porous material would be possible. Note that the later on presented homogenisation theory is not capable of describing effective elasticity of materials, which are not connected in all directions in the micro-scale.

The constructed structure is then placed at the bottom of a cavity problem (Fig. 4.1b). The lid of the cavity is driven using the same wall velocity U_w as in the two-dimensional case. Both slip velocity and penetration velocity near the poroelastic structure in this problem are very similar to those reported for the two-dimensional case (Fig. 4.2), therefore the velocity plots are not
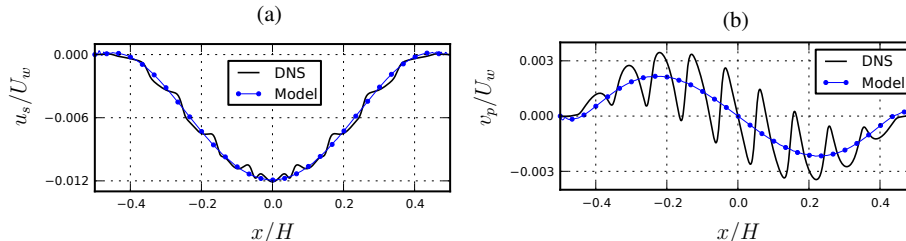
FIGURE 4.2. Results of the lid-driven cavity problem using direct numerical simulation and homogenised model for porous material. In frame (a), we show slip velocity and in frame (b), we show penetration velocity. Both velocities are sampled at coordinate $y = 0.01\,H$. Volume fraction of solid material is $2\,\%$ and scale separation parameter is $l/H = 0.1$.

reported again. We show the horizontal displacement field close to the interface in Fig. 4.3a. There we see that the horizontal displacement is very similar to the slip velocity, which essentially shows that the displacement is mostly governed by the free fluid shear at the interface. The vertical displacement shown in Fig. 4.3b, on the other hand, seems to be governed by the transfer of momentum in and out of the porous medium, as seen by the similarity between the penetration velocity and the vertical displacement. For more results and discussion of the poroelastic medium at the bottom of the cavity, see paper 5.

4.2. Velocity interface condition

In order to have a useful homogenised model of porous or poroelastic material subjected to a free fluid flow, an appropriate boundary condition is needed at the interface between the two. Theoretical approaches to model the interface condition using volume averaging or homogenisation has been proposed before. Using homogenisation approach, theoretical derivation of the stream-wise boundary condition has been carried out by Mikelić & Jäger (2000), and for the pore pressure condition by Marciniak-Czochra & Mikelić (2012). These conditions have been validated by Carraro et al. (2013) for a one-dimensional channel flow. The boundary condition for the vertical velocity component has been derived and confirmed by Carraro et al. (2015). Despite these efforts, researchers are still using empirical conditions or proposing new ones. The main reason seems to be a lack of step-by-step instructions on how to use these theoretically derived boundary conditions. Therefore we have used the homogenization via multi-scale expansion in order to derive and explain a framework, on how to get the necessary boundary conditions purely theoretically, if the geometry of the underlying porous material is known. The explanation of the method can be found in (Lācis & Bagheri 2016, paper 4). In order to make the work as widely accessible as possible, we have also released all the required codes as an open-source software (Lācis & Bagheri 2016).

The boundary condition derived in (Lācis & Bagheri 2016, paper 4) in dimensional form is

$$\mathbf{u} = -\frac{\mathbf{K}}{\mu} \cdot \nabla p^- + \mathbf{L} : \left[\nabla \mathbf{u} + (\nabla \mathbf{u})^T \right], \tag{4.1}$$

where $\mathbf{K}$ is the second-rank interface permeability tensor and $\mathbf{L}$ is the third-rank interface slip length tensor. The velocity at the interface is depending on the gradient of the pore pressure p^- and free fluid velocity strain $\nabla \mathbf{u} + (\nabla \mathbf{u})^T$. The main contribution from our work on the boundary condition (Lācis & Bagheri 2016, paper 4) is (i) showing that both velocity strain terms appear in the boundary condition and (ii) testing the derived boundary conditions in a two-dimensional setting. We note that it is important that the velocity condition contains the pore-pressure gradient, otherwise the error in interface-normal velocity might be very large (we have observed error up to 200%). Using the derived boundary condition, we were able to model the slip velocity (Fig. 4.2a) and the penetration velocity (Fig. 4.2b) with a good accuracy in an effective way, i.e., the model is not capturing the micro-scale oscillations, however, it is predicting the average macro-scale behaviour. The extension of this boundary condition to poroelastic set-up is trivial, as discussed in paper 5. Essentially, the same boundary condition holds for the relative flow velocity with respect to the motion of the solid skeleton. We trust that based on this work, researchers should be able to employ theoretically sound boundary conditions in a homogenised setting.

Note that the derivation of this boundary condition is carried out under one special assumption – that the shear from the free fluid above the porous material is of the same order as the pressure gradient, which can be estimated by assuming that the free fluid Reynolds number is of order $Re_f \sim \epsilon^{-1}$. In paper 4, we discuss that this assumption, although restrictive in nature, has only theoretical consequences. It gives a convenient way to derive generalised boundary condition of that originally proposed by Beavers & Joseph (1967), and also produces a condition, which in practice works also away from the used assumption.

4.3. Effective model equations

Although the effective elasticity equations have already been derived by Lee & Mei (1997b) and explained in the book by Mei & Vernescu (2010), we have re-examined the used assumptions and resulting equations. The derivations of the macro-scale equations and corresponding micro-scale problems can be found in the appendix of paper 5. The discussion about practical limits of the model equations can be found in the section 5 of paper 5.

The result of derivations from the appendix of paper 5 is that the homogenised solid displacement is governed by a linear law, i.e.,

$$(1 - \theta) \, \rho_s \partial_t^2 \mathbf{v} = \boldsymbol{\nabla} \cdot \left[\mathbf{C} : \frac{1}{2} \left(\boldsymbol{\nabla} \mathbf{v} + (\boldsymbol{\nabla} \mathbf{v})^T \right) - \boldsymbol{\alpha} p \right], \tag{4.2}$$
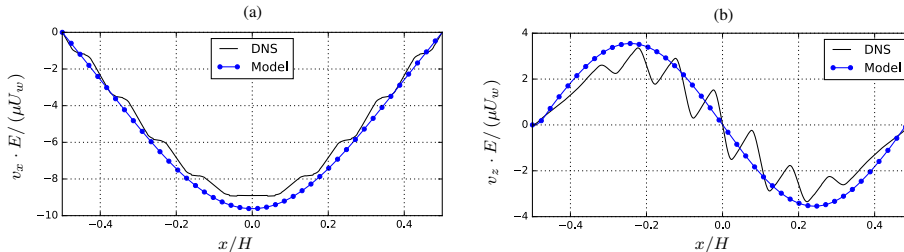
FIGURE 4.3. Results of the lid-driven cavity problem using direct numerical simulation and homogenised model for porous material. In frame (a), we show the horizontal displacement and in frame (b), we show the vertical displacement. Both fields are sampled at coordinate $z = -0.05\,H$. Volume fraction of the solid material is $14\,\%$ and the scale separation parameter is $l/H = 0.1$.

where $\theta = V_f/V$ is the porosity or fluid volume fraction, ρ_s is the solid skeleton density, $\mathbf{v}$ is the displacement field of the poroelastic material, p is the pore fluid pressure inside the poroelastic material, $\mathbf{C}$ is a fourth-rank effective elasticity tensor of the poroelastic material, and $\boldsymbol{\alpha}$ is the coefficient for the pore pressure contribution in the total stress. These effective tensors can be obtained using a set of micro-scale problems, as described in paper 5. The pore pressure, on the other hand, is governed by

$$\tilde{\mathcal{E}}\partial_t\hat{p} - \boldsymbol{\nabla}\cdot\left(\frac{\mathbf{K}}{\mu}\cdot\boldsymbol{\nabla}\hat{p}\right) = -\boldsymbol{\alpha}:\frac{1}{2}\partial_t\left(\boldsymbol{\nabla}\hat{\mathbf{v}} + (\boldsymbol{\nabla}\hat{\mathbf{v}})^T\right). \qquad (4.3)$$

Here, the scalar $\tilde{\mathcal{E}}$ characterise the solid skeleton displacement response to the time variation of pressure. The permeability tensor $\mathbf{K}$ characterises the seepage flow relationship with pressure gradient. The effective parameters in this equation are also determined by micro-scale problems, where test displacement fields are solved for. These governing equations are generalised versions of the expressions for poroelastic materials derived by Biot (1941). The solid momentum equation (4.2) in the non-inertial regime for isotropic effective elasticity tensor reduces to expression (Biot 1941, eq. 4.1), whereas the pore pressure equation (4.3) for the isotropic case reduces to expression (Biot 1941, eq. 4.4).

The governing equations in the poroelastic medium (4.2– 4.3) together with the velocity boundary condition (Lācis & Bagheri 2016, paper 4) and the total stress continuity at the interface have been implemented using the FreeFem++ (Hecht 2012) solver. The resulting software has been released as an open-source code (Lācis & Bagheri 2016). The same test problems as described in section 4.1 has been simulated. The obtained slip velocity and penetration velocity distribution over a horizontal slice near the porous structure is shown in Fig. 4.2. The agreement between direct numerical simulations and results from homogenised equations is very good, although the latter does not capture the

pore-scale variations. The solid displacement results are shown in Fig. 4.3. In the displacement comparison between the DNS and the model, one can observe that the agreement is satisfactory, although the displacement is consistently overestimated. We attribute this error to the stress interface condition, which could be improved by constructing a similar interface problem as for the velocity condition. See paper 5 for additional discussion.

4.4. Immersed boundary method for poroelastic materials

We have considered another approach to cross-reference and validate the poroelastic model results. Knowing that we already have a two-dimensional IB code, the natural question is – can this framework be used to simulate a poroelastic medium?

The most appropriate way to proceed is to resolve the shape of porous or poroelastic skeleton structure using many Lagrangian points with a good precision, taking into account the diffusive nature of the interface in IB method. This would, however, result in a very fine fluid mesh over a large domain and it is not clear if this approach would be computationally cheaper than the classical simulations using a body fitted mesh. To render IB simulations feasible, we consider a single Lagrangian point as a model for a circular cylinder. Modelling the cylinder with a single point is crude, and also it is not clear, what should be the diameter of such a "cylinder". In reality, the Lagrangian point creates a smoothed volume forcing at the neighbouring fluid nodes. We carry out numerical simulations of flow around one Lagrangian point for various Reynolds numbers and compare the obtained drag coefficient with experimental results by Tritton (1959) for different "diameters" of the IB cylinder. We found that
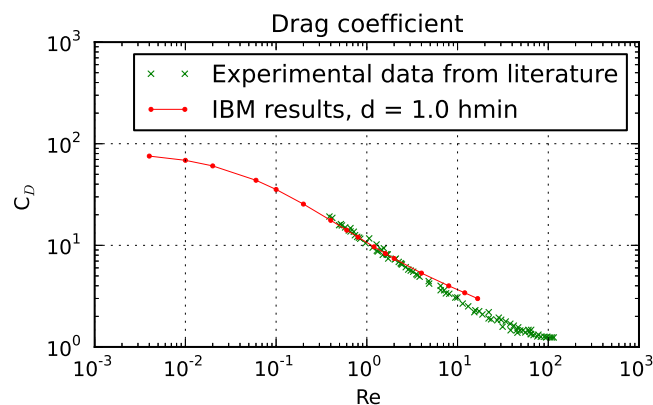

FIGURE 4.4. Direct numerical simulations of a flow over one Lagrangian point for various Reynolds numbers. The diameter of the model cylinder d is set to one mesh spacing $h_{\min}$. For comparison, literature data from Tritton (1959) is given.

the best results can be obtained, if the diameter of the cylinder is set to length of one mesh spacing $d = 1.0\,h_{\min}$. The results are shown in Fig. 4.4. From the plot one can observe that using this interpretation, the integral measure – drag coefficient – from the single Lagrangian point is very similar to that of the cylinder for a range of Reynolds numbers from around $Re = 0.5$ to around $Re = 5$. These findings indicate that a single Lagrange point might be used as a representation of a circular cylinder in certain cases. The accuracy of this representation deteriorates for smaller and larger Reynolds numbers.

The elasticity in the two-dimensional setting must be modelled, if one requires both seepage velocity and stress transfer through the medium. Therefore we introduce a spring model, i.e., we connect the neighbouring Lagrangian points using a set of linear extension and torsion springs. We carry out a steady simulation of a channel, partially obstructed by a poroelastic medium. The Reynolds number based on the channel height is around 100 and the solid volume fraction is around 1%. The vorticity field and new shape of the obstruction is shown in Fig. 4.5 (left). There we see that the poroelastic material has deformed under the pressure and shear forces from the surrounding fluid. In Fig. 4.5 (right), we show the stream-wise (horizontal) flow velocity sampled at the red line. From this plot, one can observe the characteristic velocity oscillations over the space, with the wave-length being set by the location of the Lagrange points.
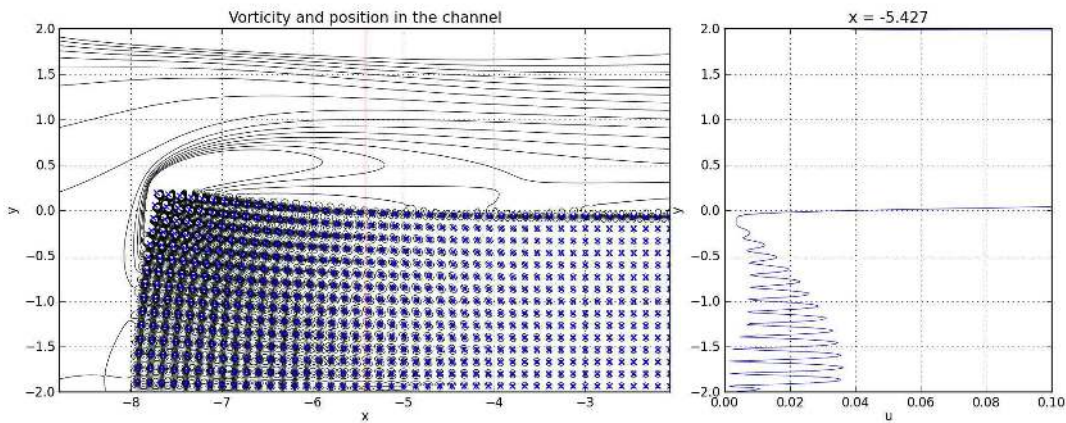

FIGURE 4.5. IB simulations of a flow over a poroelastic obstacle in a two-dimensional channel. The Reynolds number based on the channel height is around 100, and the solid volume fraction is around 1%. On the left, we show vorticity of the flow and the final shape of the obstacle. On the right, we show the stream-wise velocity profile along the slice marked by the red line.

In the future, the presented model should be further validated with respect to how accurate the flow field around a single Lagrange point in the IB method is compared to the flow field around a cylinder. The resulting flow fields and the displacement fields from the IB description of the poroelastic material should then be compared to direct numerical simulations of the whole system in order to validate the elasticity model. In addition, the code and elastic materials should be extended to three dimensions. The main advantage of this approach is that there is no separate modelling involved at the interface between the free fluid and the poroelastic material.

CHAPTER 5

Summary of the papers

Paper 1

Passive appendages generate drift through symmetry breaking

In this paper, we investigate a simple model of an appendage behind a body
– splitter plate behind a circular cylinder. We show that although generally
a recirculation region behind a body is not desirable and increases drag, some
of that lost energy can be recovered using a symmetry breaking. We show
that a short splitter plate in the wake becomes unstable in a similar man-
ner as the inverted pendulum becomes unstable under the influence of gravity,
thus we denote it as inverted-pendulum-like (IPL) instability. Although this
effect has been observed previously both for rigid and elastic appendages, the
precise mechanism and consequences remain unknown. We demonstrate the
turn and drift both experimentally (using soap-film experiments at Reynolds
number around tens of thousands) and numerically (Reynolds number around
hundred). Then we demonstrate that the IPL instability is relevant also for
elastic appendages (which are more common in nature compared to rigid ap-
pendages) and in three dimensions. We conclude that the mechanism we have
demonstrated could possibly be exploited by organisms in nature.

Paper 2

*A stable fluid-structure-interaction solver for low-density rigid particles using
the immersed boundary projection method*

In this paper, we describe the numerical method, which we developed while
working on the paper 1. We use an immersed boundary projection method as
the basis for our fluid solver and couple it with rigid body dynamics. We have
found that the explicit coupling, which is commonly used to find the solution
of a cylindrical and a spherical particle motion in fluid, becomes unstable for
bodies with non-dimensional density close to unity, if a splitter plate is added
behind the body. In order to overcome this instability, we devised an implicit
coupling scheme. We show in the paper that the implicit scheme is stable for
very light particles. We also show that the extension we have developed does
not increase the computational cost and retains a similar accuracy compared
to the original method.

Paper 3

Passive control of a falling sphere by elliptic-shaped appendages.

In this paper, we extend the investigations of the IPL instability presented in the paper 1 to a three-dimensional (3D) setting by considering a planar elliptic appendage behind a sphere. First, the intuition from a semi-quantitative IPL model developed in paper 1 for two-dimensions (2D) is introduced and later used to explain the 3D results. In this paper we use a series of flow simulations around a fixed body at various turn angles exposed to a free stream, thus imitating a steady free-fall velocity and a rotation freedom around one axis. We have limited our investigations to elliptic appendages with arbitrary aspect ratios. The total torque, drag and lift acting on the body is determined for each turn angle. The zero torque condition is used to determine the equilibrium angle, at which we obtain the drift angle as a ratio between the lift and the drag forces. By comparing the drift angle results between different aspect ratios, we identify the one which leads to a largest drift angle between the trajectory of the freely falling body and the direction of gravity. This is explained based on the intuition formed from the analysis of the IPL instability. In addition, we compare the total drag between bodies with different appendages and conclude that, for certain aspect ratios, the body experiences larger drag and slower free-fall, which can be beneficial for seed dispersal.

Paper 4

A framework for computing effective boundary conditions at the interface between free fluid and a porous medium.

In this paper, we use the method of the homogenisation via multi-scale expansion by Mei & Vernescu (2010) to derive a velocity and pressure boundary condition for a free fluid in contact with a porous medium. In the first part of the paper, we present a complete set of equations and boundary conditions needed to solve for the free fluid motion over the porous material. We illustrate the accuracy of the developed boundary condition by considering a lid-driven cavity problem, which has a porous bed consisting of circular cylinders. We compare the results from the homogenised model with the results from a fully resolved Stokes model. The corresponding numerical codes has been released as an open-source software. This part of the paper, along with the released open-source software, should be widely accessible for practitioners, who would like to use the homogenisation approach. The second part of the paper is aimed towards more theoretical readers and explains the derivation and assumptions needed to arrive with the derived boundary condition.

Paper 5

A computational continuum model of poroelastic beds.

In this paper, we continue the investigations of continuum models for free fluids over porous and poroelastic materials. Starting with Mei & Vernescu (2010), we carry out derivations of effective homogenised equations that can be used to model the behaviour of poroelastic material subjected to a moving fluid. We present the governing continuum equations for the pore pressure and poroelastic material displacement along with the necessary boundary conditions. We then present a way to determine the required effective properties, which appears in the governing equations. We employ the introduced homogenized model to describe a poroelastic material response to the free fluid vortex above it (created using the lid-driven cavity). The flow and the displacement results from the homogenised model are then compared to the results from a fully resolved simulation. From this comparison, we explain that the shear stress from the free fluid is transferred to the solid skeleton and the pore fluid in the microscale, whereas in the macroscale it is absorbed by the solid skeleton only. Consequently, we show that the stress continuity boundary condition at the interface between the free fluid and the poroelastic medium is sufficient to capture the displacement of the poroealstic medium with an acceptable accuracy. Finally, the practical limitations of the described model are discussed.

CHAPTER 6

Conclusions and outlook

In the first part of this work, we have considered a single appendage behind a bluff body and its interaction with the surrounding flow. We have looked both at solid and elastic appendages, and also both at two-dimensional and three-dimensional configurations. In those studies we observed an inverted-pendulum-like (IPL) symmetry breaking. The IPL symmetry breaking occurs if the appendage is sufficiently short with respect to the length of the back flow region; the IPL symmetry breaking causes a turn and a drift of the body. We have investigated in more detail the two-dimensional (2D) rigid case, for which we have described the turn and drift angles numerically, experimentally and also theoretically. To facilitate the 2D numerical simulations of a freely falling body, we have extended the immersed boundary (IB) projection method to include an implicit coupling between the fluid solver and the solver for Newton's equations of motion. We have determined that IPL is not an elastic instability, but a fundamental fluid-structure-interaction (FSI) instability. Carrying out this work, we have successfully reached the first objective, outlined in section 1.2.

In the second part of this work, we have investigated the method of homogenisation via multi-scale expansion to simplify the description of porous and poroelastic multi-scale materials in moving fluids. We have used the method to derive the effective boundary condition for the free fluid at the interface with porous and poroelastic material, as well as for the pore pressure. We have also derived the effective governing equations for the poroelastic material and analysed the practical limitations of those equations. We have compared the effective model predictions of the flow and the displacement fields to the results from fully resolved direct numerical simulations and observed good agreement. We have looked into the stress boundary condition for the displacement of the poroelastic material and found that the stress continuity condition provides good results. We have explained this by illustrating that the shear stress transfer from the free fluid to the pore fluid is a microscale effect, while the shear stress transfer to the poroelastic skeleton is a macroscale effect. Based on this, we justify that using the stress continuity interface condition is a good choice. With this work, we have fulfilled the second objective outlined in section 1.2.

Based on the current thesis activities, there are several directions that could be further taken in order to approach the overarching aim. One of the possible projects is to further investigate appendages in the recirculation region behind a bluff body as means to generate a favourable interaction between the

surrounding fluid and the structure. The objectives for a following doctoral student would include but are not limited to:

1. Implement an efficient numerical method for investigations of elastic one-dimensional filaments behind a freely falling body.
2. Extend the numerical implementation to three dimensions, in which elastic two-dimensional sheets (or flags) of various shapes could be described.
3. Investigate more complex appendages with holes or more than one plane; approach the shapes that can be observed in nature.
4. Look into appendage role in a swimming process, both in two- and three-dimensional setting.
5. Extend the model suited for appendage description to three-dimensions and also to include unsteady effects; investigate the applicability of different modelling approaches.

Another possible project for a following doctoral student would be to continue modelling multi-scale poroelastic materials and interaction with the surrounding moving fluid. The objectives for this student could be:

1. Develop more complex time dependent direct numerical simulations with deforming meshes that would allow validation of the homogenised model for a wider range of parameters.
2. Introduce mesh deformation also in the homogenised model setting and use the arbitrary Lagrangian-Eulerian (ALE) method to avoid mesh node displacements in tangential direction of the interface.
3. Carry out a proper treatment of stress boundary condition using multi-scale expansion and interface cells.
4. Modify the pore-scale test problems in order to account for porosity changes due to a change in pore-scale geometry, especially due to a change of the pore-scale structure volume.
5. Couple the homogenisation description of a poroelastic material to large-eddy-simulation framework for higher Reynolds number flows.
6. Apply the developed models for characterisation of turbulent flow over poroelastic structures, unsteady flow around a cylinder coated with poroelastic material and other physical problems.

To sum up, this thesis work serves as an important step in further improving the understanding and knowledge about how appendages and poroelastic materials interact with surrounding flows, which in future could lead to novel engineering applications.

Acknowledgements

The first and the foremost thanks goes to my advisor, Dr. Shervin Bagheri, who accepted me for this thesis work. Without his acceptance, this book would not have reached the daylight and everyone else on these two pages would not have had the chance to influence my scientific work. The support and guidance I have received from my advisor during all these years have exceeded my expectations in a positive way. I trust that at the end of this time, which I have spent as your doctoral student, we both have learnt from each other tremendously. I would also like to thank Dr. Fredrik Lundell for his work as my co-advisor. I have very much enjoyed our discussions on topics directly related (and also not related) to my thesis work, research or academia in general.

I appreciate the fruitful collaborations I had with researchers in France, Italy, and also here, in Stockholm. I thank Nicolas Brosse for his good work on soap-film experiments. I express my gratitude to Alessandro Bottaro, Giuseppe Antonio Zampogna, Andrea Mazzino, Stefano Olivieri and Damiano Natali for welcoming me to Genoa and making my research visit in Italy more enjoyable and productive. I also thank Kunihiko (Sam) Taira for his contribution in my understanding of numerical method development and the joint work we had on the immersed boundary projection method. I wish you all the best in your future endeavours.

Thanks to all current and past colleagues here in the Department of Mechanics, at KTH. I enjoyed the atmosphere we all have created within the Department, I am happy that you were always willing to share your resources, and open to giving advices, when I was in need. Although I have not had time to get to know the new 8th floor colleagues in Osquars backe 18, I have enjoyed what little interactions we have had. I thank the colleagues of 7th floor (which now in fact are the ones I got to know, when I was still sitting up on the 8th floor) for the good company and interesting discussions about science and life. I thank all the colleagues from 6th and 5th floor about the positive

view they have always had on everything, despite all the hard work that we have to go trough. I deeply thank Mattias for his quick help in translating the abstract in Swedish and Shervin for improving it. I am also grateful to Mattias, Sudhakar and Shervin for carefully proofreading the comprehensive summary of this thesis. I am thankful for the company of my colleagues from the lab during the supervision of undergraduate students, and also on the *innebandy* (floorball) field. In addition, I would like to thank all the anonymous referees who were and will be peer-reviewing our scientific contributions – you have made our understanding even better than it was, when we first finished the preparation of our manuscripts. Also, I express the gratitude to the opponent of this thesis and the committee members – thank you for your interest in my work and coming to Stockholm to examine it. Last, but not the least, I thank our administrative staff for helping with practical matters throughout my work as a PhD student and enabling me to focus on research and not on bureaucracy.

A special thanks goes to all Latvian people, who I have met here in Sweden. I am thankful to them for keeping my Latvian part alive by dancing in folk dance group. By taking part in our common events, I managed to get my thoughts away from science and I had the needed rest to be able to carry on.

Finally my biggest gratitude goes to my family.

The first part goes to my childhood relatives through which I was raised and developed as a personality, scientist and artist, which I am now. I thank my mother for the emotional side in me and emotional support during all this time abroad; I thank my father for the practical side in me and practical support; I thank my two sisters for not hating me after all the fights we have had in the childhood. :) I thank my *farfar* (father-father) for the nice time I had in the summerhouse in *Ogre, Latvia*; I thank my *farmor* (father-mother) for singing all the Latvian songs when I was little; I thank my *morfar* (mother-father) for discussions about physics and shaping my understanding of the world; I thank my *mormor* (mother-mother) for all discussions about life philosophy. I also thank my relatives in *Sigulda, Latvia* (cousins Indra and Edgars, aunt Vita and uncle Arturs), with whom I spend quite some unforgettable summer breaks. I wish all the worlds warmth and happiness to you!

The second part goes to my current family, my wife Iveta, my son Madars and daughter Kate. I am very happy about all the love that I have received from all of you. I thank Iveta for accepting me despite all my shortcomings and supporting me in every possible way. And I am grateful to my kids, who despite the fact that I am often very strict (especially, when you would like some extra candy before bedtime, but I would not allow that) are still happy to see me. I started my doctoral studies as a single man, but I now finish as a family man. I am happy that I had the chance to experience this change.

Thank you all! Without you, neither this thesis
nor I would be the same!

Bibliography

ABDULBARI, H., YUNUS, R., ABDURAHMAN, N. & CHARLES, A. 2013 Going against the flow—a review of non-additive means of drag reduction. *J. Ind. Eng. Chem.* **19** (1), 27–36.

ALBEN, S. & SHELLEY, M. 2005 Coherent locomotion as an attracting state for a free flapping body. *Proc. Nat. Acad. Sci. USA* **102** (32), 11163–11166.

AMESTOY, P., DUFF, I., L'EXCELLENT, J. & KOSTER, J. 2001 A fully asynchronous multifrontal solver using distributed dynamic scheduling. *SIAM J. Matrix Anal. A.* **23** (1), 15–41.

ANDERSEN, A., PESAVENTO, U. & WANG, Z. 2005*a* Analysis of transitions between fluttering, tumbling and steady descent of falling cards. *J. Fluid Mech.* **541**, 91–104.

ANDERSEN, A., PESAVENTO, U. & WANG, Z. J. 2005*b* Unsteady aerodynamics of fluttering and tumbling plates. *J. Fluid Mech.* **541**, 65–90.

ARGENTINA, M. & MAHADEVAN, L. 2005 Fluid-flow-induced flutter of a flag. *Proc. Nat. Acad. Sci. USA* **102** (6), 1829–1834.

AURIAULT, J. L. 2010*a* About the Beavers and Joseph boundary condition. *Transport Porous Med.* **83** (2), 257–266.

AURIAULT, J. L. 2010*b* Reply to the comments on "About the Beavers and Joseph boundary condition". *Transport Porous Med.* **83** (2), 269–270.

AURIAULT, J. L., GEINDREAU, C. & BOUTIN, C. 2005 Filtration law in porous media with poor separation of scales. *Transport Porous Med.* **60** (1), 89–108.

BAEK, H. & KARNIADAKIS, G. E. 2012 A convergence study of a new partitioned fluid–structure interaction algorithm based on fictitious mass and damping. *J. Comput. Phys.* **231** (2), 629 – 652.

BAGHERI, S., MAZZINO, A. & BOTTARO, A. 2012 Spontaneous symmetry breaking of a hinged flapping filament generates lift. *Phys. Rev. Lett.* **109**, 154502.

BEAVERS, G. S. & JOSEPH, D. D. 1967 Boundary conditions at a naturally permeable wall. *J. Fluid Mech.* **30** (01), 197–207.

BECHERT, D. W., BRUSE, M. & HAGE, W. 2000 Experiments with three-dimensional riblets as an idealized model of shark skin. *Experiments in fluids* **28** (5), 403–412.

BECHERT, D. W., BRUSE, M., HAGE, W., VAN DER HOEVEN, J. G. T. & HOPPE, G. 1997 Experiments on drag-reducing surfaces and their optimization with an adjustable geometry. *J. Fluid Mech.* **338**, 59–87.

BHALLA, A. P. S., BALE, R., GRIFFITH, B. E. & PATANKAR, N. A. 2013 A unified

mathematical framework and an adaptive numerical method for fluid–structure interaction with rigid, deforming, and elastic bodies. *J. Comput. Phys.* **250**, 446 – 476.

BIOT, M. A. 1941 General theory of three-dimensional consolidation. *J. Appl Phys.* **12** (2), 155–164.

BIOT, M. A. 1956 Theory of propagation of elastic waves in a fluid-saturated porous solid. I. Low-frequency range. *J. Acoust. Soc. Am.* **28** (2), 168–178.

BLACKFORD, L. S., CHOI, J., CLEARY, A., D'AZEVEDO, E., DEMMEL, J., DHILLON, I., DONGARRA, J., HAMMARLING, S., HENRY, G., PETITET, A., STANLEY, K., WALKER, D. & WHALEY, R. C. 1997 *ScaLAPACK Users' Guide*. Philadelphia, PA: Society for Industrial and Applied Mathematics.

BORAZJANI, I. 2013 Fluid–structure interaction, immersed boundary-finite element method simulations of bio-prosthetic heart valves. *Comput. Methods Appl. Mech. Eng.* **257**, 103–116.

BORAZJANI, I., GE, L. & SOTIROPOULOS, F. 2008 Curvilinear immersed boundary method for simulating fluid structure interaction with complex 3D rigid bodies. *J. Comput. Phys.* **227** (16), 7587 – 7620.

BREUGEM, W.-P. 2012 A second-order accurate immersed boundary method for fully resolved simulations of particle-laden flows. *J. Comput. Phys.* **231** (13), 4469–4498.

BRODIE, I. & MURAY, J. J. 1992 *The Physics of Micro/Nano-Fabrication*. Springer Science & Business Media.

BROSSE, N., FINMO, C., LUNDELL, F. & BAGHERI, S. 2015 Experimental study of a three-dimensional cylinder–filament system. *Exp. Fluids* **56** (6), 1–7.

CAMPBELL, R. 2013 https://www.flickr.com/photos/acrylicartist/8669674112, released under license **CC BY 2.0**.

CANO-LOZANO, J. C., BOHORQUEZ, P. & MARTÍNEZ-BAZÁN, C. 2013 Wake instability of a fixed axisymmetric bubble of realistic shape. *Int. J. Multiphas. Flow* **51**, 11–21.

CANO-LOZANO, J. C., MARTÍNEZ-BAZÁN, C., MAGNAUDET, J. & TCHOUFAG, J. 2016a Paths and wakes of deformable nearly spheroidal rising bubbles close to the transition to path instability. *Phys. Rev. Fluids* **1** (5), 053604.

CANO-LOZANO, J. C., TCHOUFAG, J., MAGNAUDET, J. & MARTÍNEZ-BAZÁN, C. 2016b A global stability approach to wake and path instabilities of nearly oblate spheroidal rising bubbles. *Phys. Fluids* **28** (1), 014102.

CAROTENUTO, C. & MINALE, M. 2013 On the use of rough geometries in rheometry. *J. Non-Newton. Fluid* **198**, 39–47.

CARRARO, T., GOLL, C., MARCINIAK-CZOCHRA, A. & MIKELIĆ, A. 2013 Pressure jump interface law for the Stokes–Darcy coupling: Confirmation by direct numerical simulations. *J. Fluid Mech.* **732**, 510–536.

CARRARO, T., GOLL, C., MARCINIAK-CZOCHRA, A. & MIKELIĆ, A. 2015 Effective interface conditions for the forced infiltration of a viscous fluid into a porous medium using homogenization. *Comput. Methods Appl. Mech. Eng.* **292**, 195–220.

CARTER, D. R. & WONG, M. 2003 Modelling cartilage mechanobiology. *Philos. T. Roy. Soc. B.* **358** (1437), 1461–1471.

CAUSIN, P., GERBEAU, J. & NOBILE, F. 2005 Added-mass effect in the design of partitioned algorithms for fluid–structure problems. *Comput. Methods Appl. Mech. Eng.* **194** (42–44), 4506 – 4527.

CHAMBERLAIN, J. A. 1976 Flow patterns and drag coefficients of cephalophod shells. *Paleontology* **19**, 539–563.

CIMBALA, J. M. & CHEN, K. T. 1994 Supercritical Reynolds number experiments on a freely rotatable cylinder/splitter plate body. *Phys. Fluids* **6** (7), 2440–2445.

COLONIUS, T. & TAIRA, K. 2008 A fast immersed boundary method using a nullspace approach and multi-domain far-field boundary conditions. *Comput. Methods Appl. Mech. Eng.* **197** (25), 2131–2146.

CONCA, C., OSSES, A. & PLANCHARD, J. 1997 Added mass and damping in fluid-structure interaction. *Comput. Methods Appl. Mech. Eng.* **146** (3–4), 387 – 405.

COUDER, Y. 1984 Two-dimensional grid turbulence in a thin liquid film. *J. Phys. Lett. - Paris* **45** (8), 353–360.

COUDER, Y., CHOMAZ, J. M. & RABAUD, M. 1989 On the hydrodynamics of soap films. *Physica D* **37** (1-3), 384–405.

COWIN, S. C. 2013 *Continuum mechanics of anisotropic materials*. Springer Science & Business Media.

CUSHMAN, J. H., BENNETHUM, L. S. & HU, B. X. 2002 A primer on upscaling tools for porous media. *Adv. Water Resour.* **25** (8), 1043–1067.

DALE, B. 2007 https://commons.wikimedia.org/wiki/File:Cessna_182_model-wingtip-vortex.jpg, released under license **CC BY-SA 3.0**.

DARCY, H. 1856 *Les fontaines publiques de la ville de Dijon: exposition et application*. Victor Dalmont.

DAVIT, Y., BELL, C., BYRNE, H., CHAPMAN, L., KIMPTON, L., LANG, G., LEONARD, K., OLIVER, J., PEARSON, N., SHIPLEY, R. *et al.* 2013 Homogenization via formal multiscale asymptotics and volume averaging: How do the two techniques compare? *Adv. Water Resour.* **62**, 178–206.

DEAN, B. & BHUSHAN, B. 2010 Shark-skin surfaces for fluid-drag reduction in turbulent flow: a review. *Philos. T. Roy. Soc. A.* **368** (1929), 4775–4806.

DEYNAT, P. 2011 https://commons.wikimedia.org/wiki/Denticules_cutan%C3%A9s_du_requin_citron_Negaprion_brevirostris_vus_au_microscope_%C3%A9lectronique_%C3%A0_balayage.jpg, released under license **CC BY-SA 3.0**.

DICKINSON, M. H., FARLEY, C. T., FULL, R. J., KOEHL, M. A. R., KRAM, R. & LEHMAN, S. 2000 How animals move: An integrative view. *Science* **288** (5463), 100–106.

DUDLEY, R., KING, V. & WASSERSUG, R. 1991 The implications of shape and metamorphosis for drag forces on a generalized pond tadpole (rana catesbeiana). *Copeia* pp. 252–257.

ELDREDGE, J. D. 2008 Dynamically coupled fluid–body interactions in vorticity-based numerical simulations. *J. Comput. Phys.* **227** (21), 9170–9194.

ERN, P., RISSO, F., FABRE, D. & MAGNAUDET, J. 2012 Wake-induced oscillatory paths of bodies freely rising or falling in fluids. *Annu. Rev. Fluid Mech.* **44**, 97–121.

FAVIER, J., DAUPTAIN, A., BASSO, D. & BOTTARO, A. 2009 Passive separation control using a self-adaptive hairy coating. *J. Fluid Mech.* **627**, 451–483.

FENG, J., HU, H. & JOSEPH, D. 1994 Direct simulation of initial value problems for

the motion of solid bodies in a Newtonian fluid. Part 2. Couette and Poiseuille flows. *J. Fluid Mech.* **277** (271), 271–301.

FENG, Z.-G. & MICHAELIDES, E. E. 2004 The immersed boundary-Lattice Boltzmann method for solving fluid–particles interaction problems. *J. Comput. Phys.* **195** (2), 602–628.

FERZIGER, J. H. & PERIĆ, M. 2002 *Computational methods for fluid dynamics.* Springer.

FISH, F. E. & LAUDER, G. V. 2006 Passive and active flow control by swimming fishes and mammals. *Annu. Rev. Fluid. Mech.* **38**, 193–224.

FLECK, N. A., DESHPANDE, V. S. & ASHBY, M. F. 2010 Micro-architectured materials: past, present and future. *P. Roy. Soc. A – Math. Phy.* **466** (2121), 2495–2516.

FORNBERG, B. 1988 Generation of finite difference formulas on arbitrarily spaced grids. *Math. Comput.* **51** (184), 699–706.

FÖRSTER, C., WALL, W. A. & RAMM, E. 2007 Artificial added mass instabilities in sequential staggered coupling of nonlinear structures and incompressible viscous flows. *Comput. Methods Appl. Mech. Eng.* **196** (7), 1278 – 1293.

GABBAI, R. & BENAROYA, H. 2005 An overview of modeling and experiments of vortex-induced vibration of circular cylinders. *J. Sound V.* **282** (3–5), 575 – 616.

GAJO, A. 2010 A general approach to isothermal hyperelastic modelling of saturated porous media at finite strains with compressible solid constituents. *P. Roy. Soc. A – Math. Phy.* **466** (2122), 3061–3087.

GAJO, A. & DENZER, R. 2011 Finite element modelling of saturated porous media at finite strains under dynamic conditions with compressible constituents. *Int. J. Numer. Meth. Eng.* **85** (13), 1705–1736.

GAZZOLA, M., ARGENTINA, M. & MAHADEVAN, L. 2014 Scaling macroscopic aquatic locomotion. *Nature Physics* **10** (10), 758–761.

GEMMELL, B. J., OH, G., BUSKEY, E. J. & VILLAREAL, T. A. 2016 Dynamic sinking behaviour in marine phytoplankton: rapid changes in buoyancy may aid in nutrient uptake. *P. Roy. Soc. B. – Biol. Sci.* **283** (1840), 20161126.

GEUZAINE, C. & REMACLE, J. F. 2009 Gmsh: A 3-D finite element mesh generator with built-in pre-and post-processing facilities. *Int. J. Numer. Meth. Eng.* **79** (11), 1309–1331.

GHARIB, M. & DERANGO, P. 1989 A liquid film (soap film) tunnel to study two-dimensional laminar and turbulent shear flows. *Physica D* **37**, 406–416.

GIBOU, F. & MIN, C. 2012 Efficient symmetric positive definite second-order accurate monolithic solver for fluid/solid interactions. *J. Comput. Phys.* **231** (8), 3246 – 3263.

GLOWINSKI, R., PAN, T.-W., HESLA, T. I. & JOSEPH, D. D. 1999 A distributed Lagrange multiplier/fictitious domain method for particulate flows. *Int. J. Multiphas. Flow* **25** (5), 755–794.

GOPINATH, A. & MAHADEVAN, L. 2011 Elastohydrodynamics of wet bristles, carpets and brushes. *P. Roy. Soc. A – Math. Phy.* p. rspa20100228.

GRIFFITH, B. E. 2012 Immersed boundary model of aortic heart valve dynamics with physiological driving and loading conditions. *Int. J. Numer. Meth. Biomed. Eng.* **28** (3), 317–345.

GUSHCHIN, V. A. & MATYUSHIN, R. V. 2006 Vortex formation mechanisms in the wake behind a sphere for $200 <$ Re < 380. *Fluid Dyn.* **41** (5), 795–809.

HAN, Y., GANATOS, P. & WEINBAUM, S. 2005 Transmission of steady and oscillatory fluid shear stress across epithelial and endothelial surface structures. *Phys. Fluids* **17** (3), 031508.

HECHT, F. 2012 New development in FreeFem++. *J. Numer. Math.* **20** (3-4), 251–265.

HUANG, W., LIU, H., WANG, F., WU, J. & ZHANG, H. P. 2013 Experimetal study of a freely falling plate with an inhomogeneous mass distribution. *Phys. Rev. E* **88** (5), 053008.

HUSSONG, J., BREUGEM, W. P. & WESTERWEEL, J. 2011 A continuum model for flow induced by metachronal coordination between beating cilia. *J. Fluid Mech.* **684** (1), 137–162.

ILIEV, O., MIKELIĆ, A. & POPOV, P. 2008 On upscaling certain flows in deformable porous media. *Multiscale Model. Sim.* **7** (1), 93–123.

ITOH, M., TAMANO, S., IGUCHI, R., YOKOTA, K., AKINO, N., HINO, R. & KUBO, S. 2006 Turbulent drag reduction by the seal fur surface. *Phys. Fluids* **18** (6), 065102.

JÄGER, W. & MIKELIĆ, A. 2009 Modeling effective interface laws for transport phenomena between an unconfined fluid and a porous medium using homogenization. *Transport Porous Med.* **78** (3), 489–508.

JÄGER, W. & MIKELIĆ, A. 2010 Letter to the editor: Comments on "About the Beavers and Joseph boundary condition". *Transport Porous Med.* **83** (2), 267–268.

JASAK, H., JEMCOV, A. & TUKOVIC, Z. 2007 OpenFOAM: A C++ library for complex physics simulations. *Int. W. Coupl. Meth. Numer. Dyn.* **1000**, 1–20.

JASAK, H. & TUKOVIC, Z. 2006 Automatic mesh motion for the unstructured finite volume method. *Trans. FAMENA* **30** (2), 1–20.

JOHNSON, T. A. & PATEL, V. C. 1999 Flow past a sphere up to a reynolds number of 300. *J. Fluid Mech.* **378**, 19–70.

JONES, I. 1973 Low reynolds number flow past a porous spherical shell. *Math. Proc. Cambridge* **73** (01), 231–238.

JURETIC, F. 2015 cfMesh v1.1. *User Guide* .

KAPELLOS, G. E., ALEXIOU, T. S. & PAYATAKES, A. C. 2012 A multiscale theoretical model for fluid flow in cellular biological media. *Int. J. Eng. Sci.* **51**, 241–271.

KARNIADAKIS, G. & SHERWIN, S. 2013 *Spectral/hp element methods for computational fluid dynamics*. Oxford University Press.

KEERTHI, M. C., RAJESHWARAN, M. S., KUSHARI, A. & DE, A. 2015 Effect of leading-edge tubercles on compressor cascade performance. *AIAA Journal* **54** (3), 912–923.

KELLAY, H., WU, X.-L. & GOLDBURG, W. 1995 Experiments with turbulent soap films. *Phys. Rev. Lett.* **74**, 3975–3978.

KEMPE, T. & FRÖHLICH, J. 2012 An improved immersed boundary method with direct forcing for the simulation of particle laden flows. *J. Comput. Phys.* **231** (9), 3663–3684.

KEYES, D. E., MCINNES, L. C., WOODWARD, C., GROPP, W., MYRA, E., PERNICE, M., BELL, J., BROWN, J., CLO, A., CONNORS, J. *et al.* 2013 Multiphysics

simulations: Challenges and opportunities. *Int. J. High Perform. C.* **27** (1), 4–83.

KIM, J., KIM, D. & CHOI, H. 2001 An immersed-boundary finite-volume method for simulations of flow in complex geometries. *J. Comput. Phys.* **171** (1), 132–150.

KIM, W., PEAUDECERF, F., BALDWIN, M. W. & BUSH, J. W. M. 2012 The hummingbird's tongue: a self-assembling capillary syphon. *P. Roy. Soc. B. – Biol. Sci.* p. rspb20121837.

LĀCIS, U. & BAGHERI, S. 2016 A framework for computing effective boundary conditions at the interface between free fluid and a porous medium. *arXiv preprint arXiv:1604.02880* .

LĀCIS, U. & BAGHERI, S. 2016 https://github.com/UgisL/flowMSE.

LĀCIS, U., BROSSE, N., INGREMEAU, F., MAZZINO, A., LUNDELL, F., KELLAY, H. & BAGHERI, S. 2014 Passive appendages generate drift through symmetry breaking. *Nat. Commun.* **5**.

LĀCIS, U., TAIRA, K. & BAGHERI, S. 2016 A stable fluid–structure-interaction solver for low-density rigid bodies using the immersed boundary projection method. *J. Comput. Phys.* **305**, 300–318.

LE BARS, M. & GRAE WORSTER, M. 2006 Interfacial conditions between a pure fluid and a porous medium: implications for binary alloy solidification. *J. Fluid Mech.* **550**, 149–173.

LEE, C. K. 2004 Flow and deformation in poroelastic media with moderate load and weak inertia. *P. Roy. Soc. A – Math. Phy.* **460** (2047), 2051–2087.

LEE, C. K. & MEI, C. C. 1997a Re-examination of the equations of poroelasticity. *Int. J. Eng. Sci.* **35** (4), 329–352.

LEE, C. K. & MEI, C. C. 1997b Thermal consolidation in porous media by homogenization theory—I. Derivation of macroscale equations. *Adv. Water Resour.* **20** (2), 127–144.

LEE, C. K. & MEI, C. C. 1997c Thermal consolidation in porous media by homogenization theory—II. Calculation of effective coefficients. *Adv. Water Resour.* **20** (2), 145–156.

LIU, K. & JIANG, L. 2011 Bio-inspired design of multiscale structures for function integration. *Nano Today* **6** (2), 155–175.

LYDZBA, D. & SHAO, J. F. 2000 Study of poroelasticity material coefficients as response of microstructure. *Mech. Cohes.-Frict. Mat.* **5** (2), 149–171.

MARCINIAK-CZOCHRA, A. & MIKELIĆ, A. 2012 Effective pressure interface law for transport phenomena between an unconfined fluid and a porous medium using homogenization. *Multiscale Model. Sim.* **10** (2), 285–305.

MAVKO, G., MUKERJI, T. & DVORKIN, J. 2009 *The rock physics handbook: Tools for seismic analysis of porous media*. Cambridge university press.

MEI, C. C. & VERNESCU, B. 2010 *Homogenization methods for multiscale mechanics*. World scientific.

MEYER, R., HAGE, W., BECHERT, D. W., SCHATZ, M., KNACKE, T. & THIELE, F. 2007 Separation control by self-activated movable flaps. *AIAA journal* **45** (1), 191–199.

MIKELIĆ, A. & JÄGER, W. 2000 On the interface boundary condition of Beavers, Joseph, and Saffman. *SIAM J. Appl. Math.* **60** (4), 1111–1127.

MIKLOSOVIC, D. S., MURRAY, M. M., HOWLE, L. E. & FISH, F. E. 2004 Leading-edge tubercles delay stall on humpback whale (Megaptera novaeangliae) flippers. *Phys. Fluids* **16** (5), L39–L42.

MINALE, M. 2014*a* Momentum transfer within a porous medium. I. Theoretical derivation of the momentum balance on the solid skeleton. *Phys. Fluids* **26** (12), 123101.

MINALE, M. 2014*b* Momentum transfer within a porous medium. II. Stress boundary condition. *Phys. Fluids* **26** (12), 123102.

MOUKALLED, F., MANGANI, L. & DARWISH, M. 2015 *The Finite Volume Method in Computational Fluid Dynamics: An Advanced Introduction with OpenFOAM and Matlab*, 1st edn. Springer Publishing Company, Incorporated.

MURAD, M. A., GUERREIRO, J. N. & LOULA, A. F. D. 2001 Micromechanical computational modeling of secondary consolidation and hereditary creep in soils. *Comput. Methods Appl. Mech. Eng.* **190** (15), 1985–2016.

NAMKOONG, K., YOO, J. Y. & CHOI, H. G. 2008 Numerical analysis of two-dimensional motion of a freely falling circular cylinder in an infinite fluid. *J. Fluid Mech.* **604**, 33–53.

NIELD, D. 2009 The Beavers–Joseph boundary condition and related matters: a historical and critical note. *Transport Porous Med.* **78** (3), 537–540.

NIU, X., SHU, C., CHEW, Y. & PENG, Y. 2006 A momentum exchange-based immersed boundary-Lattice Boltzmann method for simulating incompressible viscous flows. *Phys. Lett. A* **354** (3), 173–182.

OCHOA-TAPIA, J. A. & WHITAKER, S. 1995 Momentum transfer at the boundary between a porous medium and a homogeneous fluid–I. Theoretical development. *Int. J. Heat Mass Tran.* **38** (14), 2635–2646.

OEFFNER, J. & LAUDER, G. V. 2012 The hydrodynamic function of shark skin and two biomimetic applications. *J. Exp. Biol.* **215** (5), 785–795.

OPENFOAM 2015 The Open Source CFD Toolbox. *User Guide* .

PARK, H., BAE, K., LEE, B., JEON, W.-P. & CHOI, H. 2010 Aerodynamic performance of a gliding swallowtail butterfly wing model. *Exp. Mech.* **50**, 1313–1321.

PARKER, G. A. & SMITH, J. M. 1990 Optimality theory in evolutionary biology. *Nature* **348** (6296), 27–33.

PEROT, J. 1993 An analysis of the fractional step method. *J. Comput. Phys.* **108** (1), 51–58.

PESAVENTO, U. & WANG, Z. J. 2004 Falling paper: Navier-stokes solutions, model of fluid forces, and center of mass elevation. *Phys. Rev. Lett.* **93** (14), 144501.

PESKIN, C. S. 1972 Flow patterns around heart valves: a numerical method. *J. Comput. Phys.* **10** (2), 252–271.

PESKIN, C. S. 1977 Numerical analysis of blood flow in the heart. *J. Comput. Phys.* **25** (3), 220–252.

PORTUGAL, S. J., HUBEL, T. Y., FRITZ, J., HEESE, S., TROBE, D., VOELKL, B., HAILES, S., WILSON, A. M. & USHERWOOD, J. R. 2014 Upwash exploitation and downwash avoidance by flap phasing in ibis formation flight. *Nature* **505** (7483), 399–402.

PRANDTL, L. 1905 Uber Flussigkeitsbewegung bei sehr kleiner Reibung. *Verhandlungen des dritten internationalen Mathematiker-Kongresses in Heidelberg* .

PRIDE, S. R. & BERRYMAN, J. G. 2003 Linear dynamics of double-porosity dual-permeability materials. I. Governing equations and acoustic attenuation. *Phys. Rev. E* **68** (3), 036603.

RASTEGARI, A. & AKHAVAN, R. 2015 On the mechanism of turbulent drag reduction with super-hydrophobic surfaces. *J. Fluid Mech.* **773**, R4.

ROMA, A. M., PESKIN, C. S. & BERGER, M. J. 1999 An adaptive version of the immersed boundary method. *J. Comput. Phys.* **153** (2), 509–534.

ROSTI, M., CORTELEZZI, L. & QUADRIO, M. 2015 Direct numerical simulation of turbulent channel flow over porous walls. *J. Fluid Mech.* **784**, 396–442.

ROUIFED, S., PUIJALON, S., VIRICEL, M.-R. & PIOLA, F. 2011 Achene buoyancy and germinability of the terrestrial invasive Fallopia×bohemica in aquatic environment: A new vector of dispersion? *Ecoscience* **18** (1), 79–84.

SAFFMAN, P. 1971 On the boundary condition at the surface of a porous medium. *Stud. Appl. Math.* **50** (2), 93–101.

SARPKAYA, T. 2004 A critical review of the intrinsic nature of vortex-induced vibrations. *J. Fluid. Struct.* **19** (4), 389–447.

SCHEIBE, T. D., MURPHY, E. M., CHEN, X., RICE, A. K., CARROLL, K. C., PALMER, B. J., TARTAKOVSKY, A. M., BATTIATO, I. & WOOD, B. D. 2015 An analysis platform for multiscale hydrogeologic modeling with emphasis on hybrid multiscale methods. *Groundwater* **53** (1), 38–56.

SCHWAGER, H., MASSELTER, T., SPECK, T. & NEINHUIS, C. 2013 Functional morphology and biomechanics of branch–stem junctions in columnar cacti. *P. Roy. Soc. B. – Biol. Sci.* **280** (1772), 20132244.

SELVADURAI, A. P. S. & KIM, J. 2016 Poromechanical behaviour of a surficial geological barrier during fluid injection into an underlying poroelastic storage formation. *P. Roy. Soc. A – Math. Phy.* **472** (2187).

SELVADURAI, A. P. S. & SUVOROV, A. P. 2012 Boundary heating of poro-elastic and poro-elasto-plastic spheres. *P. Roy. Soc. A – Math. Phy.* **468** (2145), 2779–2806.

SHELLEY, M. J. & ZHANG, J. 2011 Flapping and bending bodies interacting with fluid flows. *Ann. Rev. Fluid Mech.* **43**, 449–465.

SIMPSON, G., SPIEGELMAN, M. & WEINSTEIN, M. I. 2010a A multiscale model of partial melts: 1. Effective equations. *J. Geophys. Res. – Sol. Ea.* **115** (B4).

SIMPSON, G., SPIEGELMAN, M. & WEINSTEIN, M. I. 2010b A multiscale model of partial melts: 2. Numerical results. *J. Geophys. Res. – Sol. Ea.* **115** (B4).

SIROVICH, L. & KARLSSON, S. 1997 Turbulent drag reduction by passive mechanisms. *Nature* **388**, 753–755.

SKOTHEIM, J. M. & MAHADEVAN, L. 2005 Physical limits and design principles for plant and fungal movements. *Science* **308** (5726), 1308–1310.

TAIRA, K. & COLONIUS, T. 2007 The immersed boundary method: A projection approach. *J. Comput. Phys.* **225** (2), 2118–2137.

TCHOUFAG, J., FABRE, D. & MAGNAUDET, J. 2015 Weakly nonlinear model with exact coefficients for the fluttering and spiraling motion of buoyancy-driven bodies. *Phys. Rev. Lett.* **115** (11), 114501.

TOMBOULIDES, A. G., ORSZAG, S. A. & KARNIADAKIS, G. E. 1993 Direct and large-eddy simulations of axisymmetric wakes. In *31st AIAA Aerospace Sciences Meeting and Exhibit*.

TRAN, T., CHAKRABORTY, P., GUTTENBERG, N., ALISIA PRESCOTT4, H. K., GOLD-BURG, W., GOLDENFELD, N. & GIOIA, G. 2010 Macroscopic effects of the spectral structure in turbulent flows. *Nature Phys.* **6**, 438–441.

TRETHEWAY, D. C. & MEINHART, C. D. 2002 Apparent fluid slip at hydrophobic microchannel walls. *Phys. Fluids* **14** (3), L9–L12.

TRITTON, D. J. 1959 Experiments on the flow past a circular cylinder at low Reynolds numbers. *J. Fluid Mech.* **6** (04), 547–567.

TSENG, Y.-H. & FERZIGER, J. H. 2003 A ghost-cell immersed boundary method for flow in complex geometry. *J. Comput. Phys.* **192** (2), 593–623.

UHLMANN, M. 2005 An immersed boundary method with direct forcing for the simulation of particulate flows. *J. Comput. Phys.* **209** (2), 448–476.

USHIDA, A., HASEGAWA, T., NAKAJIMA, T., UCHIYAMA, H. & NARUMI, T. 2012 Drag reduction effect of nanobubble mixture flows through micro-orifices and capillaries. *Exp. Therm. Fluid. Sci.* **39**, 54–59.

VAEZI, M., SEITZ, H. & YANG, S. 2013 A review on 3D micro-additive manufacturing technologies. *Int. J. Adv. Manuf. Tech.* **67** (5-8), 1721–1754.

VALDÉS-PARADA, F. J., AGUILAR-MADERA, C. G., OCHOA-TAPIA, J. A. & GOYEAU, B. 2013 Velocity and stress jump conditions between a porous medium and a fluid. *Adv. Water Resour.* **62**, 327–339.

VOGEL, S. 1994 *Life in moving fluids: the physical biology of flow*. Princeton University Press.

WANG, C. & ELDREDGE, J. D. 2015 Strongly coupled dynamics of fluids and rigid-body systems with the immersed boundary projection method. *J. Comput. Phys.* **295**, 87–113.

WANG, Z. J., BIRCH, J. M. & DICKINSON, M. H. 2004 Unsteady forces and flows in low reynolds number hovering flight: two-dimensional computations vs robotic wing experiments. *J. Exp. Biol.* **207** (3), 449–460.

WEI, Z., NEW, T. H. & CUI, Y. D. 2015 An experimental study on flow separation control of hydrofoils with leading-edge tubercles at low Reynolds number. *Ocean Eng.* **108**, 336–349.

WHITAKER, S. 1986*a* Flow in porous media I: A theoretical derivation of Darcy's law. *Transport Porous Med.* **1** (1), 3–25.

WHITAKER, S. 1986*b* Flow in porous media III: Deformable media. *Transport Porous Med.* **1** (2), 127–154.

WHITAKER, S. 1988 Levels of Simplification. The Use of Assumptions, Restrictions, and Constraints in Engineering Analysis. *Chem. Eng. Edu.* **22** (2), 104–8.

WHITAKER, S. 1996 The Forchheimer equation: a theoretical development. *Transport Porous Med.* **25** (1), 27–61.

WHITAKER, S. 1998 *The method of volume averaging*. Springer.

WILLIAMSON, C. & GOVARDHAN, R. 2004 Vortex-induced vibrations. *Annu. Rev. Fluid Mech.* **36**, 413–455.

WOOD, B. D. 2009 The role of scaling laws in upscaling. *Adv. Water Resour.* **32** (5), 723–736.

XU, J. C., SEN, M. & GAD-EL HAK, M. 1990 Low-Reynolds number flow over a rotatable cylinder–splitter plate body. *Phys. Fluids* **2** (11), 1925–1927.

YANG, J. & STERN, F. 2015 A non-iterative direct forcing immersed boundary

method for strongly-coupled fluid–solid interactions. *J. Comput. Phys.* **295**, 779–804.

YE, T., MITTAL, R., UDAYKUMAR, H. & SHYY, W. 1999 An accurate cartesian grid method for viscous incompressible flows with complex immersed boundaries. *J. Comput. Phys.* **156** (2), 209–240.

ZAMPOGNA, G. A. & BOTTARO, A. 2016 Fluid flow over and through a regular bundle of rigid fibres. *J. Fluid Mech.* **792**, 5–35.

ZHANG, J., CHILDRESS, S., LIBCHABER, A. & SHELLEY, M. 2000 Flexible filaments in a flowing soap film as a model for one-dimensional flags in a two-dimensional wind. *Nature* **408** (6814), 835–839.

ZHENG, X., XUE, Q., MITTAL, R. & BEILAMOWICZ, S. 2010 A coupled sharp-interface immersed boundary-finite-element method for flow-structure interaction with application to human phonation. *J. Biomech. Eng.-T. ASME* **132** (11), 111003.